JCI insight

# A tryptophan-derived uremic metabolite-Ahr-Pdk4 axis governs skeletal muscle mitochondrial energetics in chronic kidney disease

Trace Thome, … , Salvatore T. Scali, Terence E. Ryan

*JCI Insight.* 2024. https://doi.org/10.1172/jci.insight.178372.

Research In-Press Preview Muscle biology Nephrology

## Graphical abstract

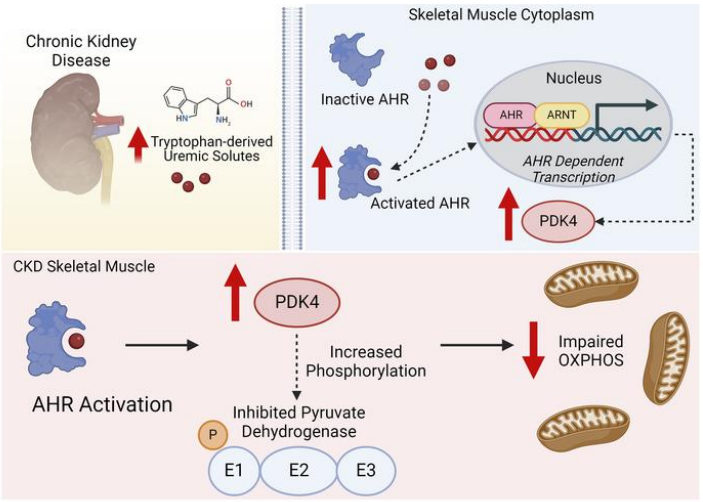

# A tryptophan-derived uremic metabolite-Ahr-Pdk4 axis governs skeletal muscle mitochondrial energetics in chronic kidney disease

Trace Thome[1], Nicholas A. Vugman[1], Lauren E. Stone[1], Keon Wimberly[1], Salvatore T. Scali[2,5], Terence E. Ryan[1,3,4,#]

[1]Department of Applied Physiology and Kinesiology, [2]Division of Vascular Surgery and Endovascular Therapy, [3]Myology Institute, [4]Center for Exercise Science, University of Florida, Gainesville, FL, USA.

[5]Malcom Randall VA Medical Center, Gainesville, FL, USA.

#Correspondence should be addressed to Terence E. Ryan, PhD: 1864 Stadium Rd, Gainesville, FL, 32611. Tel: 352-294-1700 (office); email: ryant@ufl.edu

Running Head: AHR activation and muscle mitochondria in CKD

**Conflict of Interest:** The authors have declared that no conflicts of interest exist.

## ABSTRACT

Chronic kidney disease (CKD) causes an accumulation of uremic metabolites that negatively impact skeletal muscle function. Tryptophan-derived uremic metabolites are agonists of the aryl hydrocarbon receptor (AHR) which has been shown to be activated in the blood of CKD patients. This study investigated the role of the AHR in skeletal muscle pathology of CKD. Compared to control participants with normal kidney function, AHR-dependent gene expression (*CYP1A1* and *CYP1B1*) was significantly upregulated in skeletal muscle of patients with CKD ($P$=0.032) and the magnitude of AHR activation was inversely correlated with mitochondrial respiration ($P$<0.001). In mice with CKD, muscle mitochondrial oxidative phosphorylation (OXPHOS) was significantly impaired and strongly correlated with both the serum level of tryptophan-derived uremic metabolites and AHR activation. Muscle-specific deletion of the AHR significantly improved mitochondrial OXPHOS in male mice with the greatest uremic toxicity (CKD+probenecid) and abolished the relationship between uremic metabolites and OXPHOS. The uremic metabolite-AHR-mitochondrial axis in skeletal muscle was further confirmed using muscle-specific AHR knockdown in C57BL6J that harbour a high-affinity AHR allele, as well as ectopic viral expression of constitutively active mutant AHR in mice with normal renal function. Notably, OXPHOS changes in $AHR^{mKO}$ mice were only present when mitochondria were fueled by carbohydrates. Further analyses revealed that AHR activation in mice led to significant increases in Pdk4 expression ($P$<0.05) and phosphorylation of pyruvate dehydrogenase enzyme ($P$<0.05). These findings establish a uremic metabolite-AHR-Pdk4 axis in skeletal muscle that governs mitochondrial deficits in carbohydrate oxidation during CKD.

## INTRODUCTION

Chronic kidney disease (CKD) affects over ~500 million people globally (1). CKD results in a progressive skeletal myopathy characterized by reduced muscle mass and strength, increased fatiguability, and exercise intolerance (2-5). The imbalance between muscle catabolic and anabolic pathways have been well-documented in CKD, including the overactivation of the ubiquitin proteasome system, dysregulation of autophagy, increased caspase and calpains, and impaired insulin growth like factor 1 (IGF-1) signaling which manifests as severe muscle wasting (6-15). Recently, skeletal muscle mitochondrial and redox abnormalities have emerged as potential causal factors driving the skeletal myopathy in CKD (2, 16-28), however the mechanisms governing metabolic changes are not fully understood.

The accumulation of uremic metabolites and solutes is considered a hallmark of CKD and have deleterious effects to multiple tissues (29-32). Indoxyl sulfate (IS), a well-known uremic metabolite, has been shown to impair mitochondrial respiration, increase oxidative stress, and result in muscle atrophy in mice with normal kidney function (26, 27, 33). Kynurenines are another class of uremic metabolites that accumulate in CKD patients and have been associated with low walking speed, grip strength, and frailty in non-CKD adults (34-36). Both indoles and kynurenines are derived from tryptophan catabolism and, interestingly, are ligands for the aryl hydrocarbon receptor (AHR) (37, 38), a ubiquitously expressed ligand activated transcription factor involved in xenobiotic metabolism of both endogenous and exogenous molecules (39, 40). Chronic AHR activation, primarily studied in the context of exposure to dioxin, is toxic in the liver, reproductive organs, immune system, and central nervous system (39, 41-43). These

toxic effects have been associated with disruption of circadian rhythm, metabolic syndrome, and type II diabetes (42, 44, 45). Elevated levels of AHR activation have been identified in the blood of CKD patients (46) and in several tissues of rodents with CKD(47). In skeletal muscle, recent work has shown that AHR activation phenocopies the skeletal myopathy caused by tobacco smoking (48) and contributes to worsened myopathy outcomes in the context of limb ischemia (49). Based on the prior evidence, this study aimed to test whether AHR activation links the accumulation of uremic metabolites to muscle dysfunction in CKD.

## RESULTS

***AHR activation is present in skeletal muscle of human patients and rodents with CKD.*** Several uremic metabolites that accumulate in the serum of CKD patients are derived from tryptophan catabolism (50-53) (**Figure 1A**). To explore if the accumulation of tryptophan-derived uremic metabolites results in AHR activation in skeletal muscle, we employed quantitative PCR (qPCR) to measure the mRNA expression of the *AHR* and downstream cytochrome P450 genes*, CYP1A1* and *CYP1B1,* in gastrocnemius muscle from participants with and without CKD. *AHR* and *CYP1A1* mRNA expression were increased ~11.5 and ~10.3-fold in muscle from CKD patients when compared to controls (**Figure 1B**). *CYP1B1* was increased ~6.6-fold in CKD, but this was not statistically significant (*P*=0.525) (**Figure 1B**). The expression of *CYP1A1* (a surrogate for AHR activation) had a significant inverse association with muscle mitochondrial respiration rates in permeabilized myofibers (**Figure 1C**). Immunoblotting performed on the quadriceps muscle of mice confirmed the presence of the AHR protein, although

abundance was not impacted by CKD and was lower than the liver (**Figure 1D**). Next, cultured murine (C2C12) myotubes treated with 100μM of tryptophan-derived uremic metabolites (IS, kynurenic acid (KA), L-kynurenine (L-Kyn), and indole-acetic acid (IAA)) displayed increases in *Cyp1a1* mRNA expression (**Figure 1E**). These data demonstrate that the AHR is expressed in human and mouse skeletal muscle and activated in the context of CKD and by tryptophan-derived uremic metabolites.

***Uremic metabolite accumulation drives skeletal muscle AHR activation in CKD and can be disrupted by muscle-specific AHR deletion.*** To determine if serum levels of uremic metabolites are responsible for AHR activation in skeletal muscle, we generated an inducible skeletal muscle-specific knockout mouse ($AHR^{mKO}$). Deletion of the AHR was confirmed in skeletal muscle by DNA recombination (**Supplemental Figure 2A**) and the ablation of AHR signaling (*Cyp1a1* mRNA expression) in muscle exposed to IS (**Supplemental Figure 2B**). Next, we explored the link between uremic metabolite accumulation and AHR activation using wildtype littermates ($AHR^{fl/fl}$) and $AHR^{mKO}$ mice fed either a casein control (Con) or adenine-supplemented diet (CKD), as well as CKD-mice treated twice daily with probenecid, an organic anion transporter inhibitor which has been shown to further increase uremic metabolite levels by preventing tubular secretion (54) (**Figure 2A**). L-Kyn, KA, and the L-Kyn to tryptophan ratio (Kyn/Tryp) were all significantly elevated in probenecid treated male mice with CKD (**Figure 2B**). Interestingly, kynurenine concentrations remained unchanged in females while KA and Kyn/Tryp were significantly elevated in both CKD only and probenecid groups (**Figure 2C**). *Cyp1a1* and *Ahrr* (genes regulated by the AHR) were significantly increased in

muscle from $AHR^{fl/fl}$ male mice and unaffected in the $AHR^{mKO}$ mice (**Figure 2D**). However, females elicited lower activation of AHR dependent genes compared to males (**Figure 2E**). These sex-dependent effects appear to be independent of the severity of CKD as both males and females displayed similar glomerular filtration rates (GFR, **Supplemental Figure 2C**) and blood urea nitrogen levels (**Supplemental Figure 2D**).

***Deletion of the AHR disrupts uremia induced mitochondrial OXPHOS dysfunction in skeletal muscle.*** Next, we sought to determine if the significant association between *CYP1A1* expression levels and mitochondrial respiratory function observed in skeletal muscle from patients with and without CKD (**Figure 1C**) was mediated by the AHR. Mitochondria were isolated from the muscle of $AHR^{fl/fl}$ and $AHR^{mKO}$ mice and respirometry was performed using a creatine kinase (CK) clamp to titrate the extra mitochondrial ATP/ADP ratio ($\Delta G_{ATP}$, a representation of cellular energy demand). The relationship between $\Delta G_{ATP}$ and oxygen consumption ($JO_2$) represents the conductance through the mitochondrial OXPHOS system (**Figure 3A**). Using a mixture of carbohydrate and fatty acid to fuel mitochondria, $JO_2$ and OXPHOS conductance was significantly decreased in mice with CKD (**Figure 3B**). However, deletion of the AHR did not significantly improve OXPHOS in CKD mice (**Figure 3B**). When probenecid was administered to mice with CKD to increase uremic metabolite levels and AHR activation in skeletal muscle further, deletion of the AHR was found to have sex- and fuel source-dependent effects on muscle mitochondrial OXPHOS. Under these conditions, $AHR^{mKO}$ failed to protect females from OXPHOS impairment when mitochondria were fueled by a mixture of carbohydrates and fatty acid (**Figure 3C**), consistent with the results in CKD mice without probenecid

155 treatment. However, when mitochondria were energized with carbohydrates (pyruvate
156 and malate), male $AHR^{mKO}$ mice had significantly higher OXPHOS conductance
157 compared to $AHR^{fl/fl}$ littermates ($P$=0.045 **Figure 3D**). No significant effect of $AHR^{mKO}$ was
158 observed when mitochondria were fueled only with the medium chain fatty acid
159 octanoylcarnitine in males (**Figure 3E**) or in any condition in female mice (**Figure 3C-E**).
160 Interestingly, elevated mRNA expression of pyruvate dehydrogenase kinase 4
161 (*Pdk4*), a negative regulator of pyruvate metabolism, was upregulated in male $AHR^{fl/fl}$
162 mice with CKD+probenecid but not $AHR^{mKO}$ mice (**Supplemental Figure 3A**), which
163 could explain the protection of OXPHOS observed in $AHR^{mKO}$ mice when pyruvate is the
164 primary carbon source. Mitochondrial $H_2O_2$ production was unaffected by the presence
165 of CKD or the deletion of the AHR in either sex (**Supplemental Figure 3B**). Additionally,
166 probenecid treatment alone did not have an impact on OXPHOS conductance in skeletal
167 muscle mitochondria (**Supplemental Figure 4**). We observed strong inverse correlations
168 between uremic metabolite levels (Kyn/Trp ratio and Kyn concentration) or AHR activation
169 (*Ahrr* expression) and OXPHOS conductance in male $AHR^{fl/fl}$ mice, but not in females
170 (**Figure 3F**). Interestingly, those relationships were abolished in $AHR^{mKO}$ male mice.
171 These findings agree with the observed relationship between AHR activation and $JO_2$ in
172 human CKD skeletal muscle (**Figure 1C**) and previous work in non-CKD rodents exposed
173 to elevated kynurenines (55). While CKD decreased muscle mass, myofiber size/area,
174 grip strength, and isometric contractile performance, deletion of the AHR did not attenuate
175 these changes in either sex (**Supplemental Figures 5 and 6**).
176

***Muscle-specific knockdown of the AHR in CKD mice expressing a high-affinity AHR allele improves mitochondrial OXPHOS.*** While the AHR is well conserved across species, naturally occurring polymorphisms in the sequence exist and confer differences in the affinity for ligands (56-58). The $AHR^{fl/fl}$ mice used to generate the $AHR^{mKO}$ mice herein were derived from 129-SvJ embryonic stem cells which harbor a low affinity $AHR^{d}$ allele that exhibits 10-100-fold lower sensitivity to xenobiotic ligands when compared to mice with the high-affinity $AHR^{b}$ found in C57BL/6J mice (56) (**Figure 4A**). Thus, we examined if knockdown of the AHR in muscle of C57BL/6J mice that harbor the high-affinity AHR allele would attenuate muscle pathology in CKD. Muscle-specific knockdown of the AHR was induced by systemic delivery of muscle-trophic adeno-associated virus (MyoAAV) (59) encoding a short hairpin RNA sequence targeting the AHR (shAHR) to mice with CKD (**Figure 4B**). Compared to CKD mice that received MyoAAV-GFP (green fluorescent protein), *Ahr, Cyp1a1,* and *Ahrr* mRNA levels were significantly reduced in the skeletal muscle of CKD mice that received MyoAAV-shAHR (**Figure 4C**). No differences were observed in AHR mRNA levels in the liver (**Supplemental Figure 7A**). Examination of mitochondrial function in the gastrocnemius muscle (**Figure 4D**) revealed significantly higher mitochondrial OXPHOS in male CKD mice that received MyoAAV-shAHR when mitochondria were fueled by a mixture of carbohydrate and fatty acid substrates, as well as carbohydrates only (both $P<0.01$), but not when energized with octanoylcarnitine alone (**Figure 4E,F**). Consistent with results from low-affinity $AHR^{mKO}$ mice, MyoAAV-shAHR had no effect on mitochondrial OXPHOS in female mice (**Figure 4G,H**). Mitochondrial $H_2O_2$ production, muscle mass, and muscle contractile function were not different between treatment groups (**Supplemental Figure 7**).

***Skeletal muscle-specific expression of a constitutively active AHR (CAAHR) in mice with normal kidney function impairs mitochondrial energetics.*** To isolate the role of AHR activation from the complex milieu of renal insufficiency, we generated a mutant AHR that displays constitutive transcriptional activity in the absence of ligands (60) (termed CAAHR herein). The CAAHR, or a GFP control, was delivered to mice with normal renal function using AAV9 and the skeletal muscle-specific promoter (human skeletal actin (HSA); ACTA1 gene) (**Figure 5A**). Constitutive AHR activation was confirmed via *Ahr*, *Cyp1a1*, and *Ahrr* mRNA expression (**Figure 5B**). Interestingly, *Cyp1a1* expression was higher in females than males treated with AAV-CAAHR, but this was not caused by sex-dependent differences in *Ahr* repression as *Ahrr* expression was similar between males and females (**Figure 5B**). Skeletal muscle OXPHOS function was significantly lower in AAV-CAAHR mice compared to AAV-GFP mice, regardless of sex (**Figure 5C,D**). Mitochondrial $H_2O_2$ production was unaffected by AAV-CAAHR treatment (**Figure 5E**). To explore the mechanisms underlying OXPHOS dysfunction coincident with AHR activation, we assayed several matrix dehydrogenase enzymes. AAV-CAAHR reduced the activity of pyruvate dehydrogenase (PDH), malic enzyme (ME) and aconitase in males (**Figure 5F**). In females, AAV-CAAHR decreased the activity of PDH, alpha-ketoglutarate dehydrogenase, and fumarate hydratase, but increased glutamate dehydrogenase (GDH) activity (**Figure 5F**). Additional dehydrogenase assays that were unaffected by CAAHR are shown in **Supplemental Figure 8**. Unexpectedly, AAV-CAAHR hastened muscle fatigue in male mice (**Figure 5G**) but did not affect muscle mass or strength in either sex (**Supplemental Figure 8**).

***Ahr activation drives Pdk4-induced phosphorylation of the pyruvate dehydrogenase enzyme.*** As OXPHOS function was altered by AHR activation primarily when pyruvate was supplied as a fuel source, we explored if post-translational modification of the PDH enzyme could be linked to AHR activation. The activity of PDH is regulated by its phosphorylation status, where pyruvate dehydrogenase kinases (PDKs) decrease activity and pyruvate dehydrogenase phosphatases (PDPs) increase activity. qPCR for PDK and PDP genes in skeletal muscle revealed a significant increase in the mRNA expression of *Pdk4* in both male and female mice treated with AAV-CAAHR, while other PDK isoforms (*Pdk1, Pdk2, Pdk3*) were unaltered (**Figure 6A**). Male mice treated with AAV-CAAHR had increased *Pdp1* expression (**Figure 6A**), suggesting a possible compensatory response to elevated *Pdk4*. Using assay for transposase-accessible chromatin (ATAC) sequencing to explore chromatin accessibility, there were more than 10,000 differentially accessible peaks between AAV-CAAHR and AAV-GFP muscle (**Figure 6B**). Accessibility to the promoter region of *Pdk4* was noticeably different between AAV-CAAHR and AAV-GFP muscle (**Figure 6C**).

Next, we performed immunoblotting experiments to examine PDK4 protein abundance and the phosphorylation status of the PDH enzyme. In male and female mice treated with AAV-CAAHR, PDK4 protein abundance and phosphorylation of PDHE1α at serine 300 were significantly increased compared to AAV-GFP treated mice (**Figure 6D,E**). No changes in total PDHE1α protein content were observed in either sex (**Figure 6D,E**). Additionally, we performed experiments on non-CKD control mice (Con), mice with CKD treated with MyoAAV-GFP treated, and mice with CKD treated with MyoAAV-shAHR

(only male analyses are shown due to no improvements found in OXPHOS of female MyoAAV-shAHR mice, Figure 4). MyoAAV-GFP mice with CKD had elevated PDK4 protein abundance and increased phosphorylation of PDHE1α at serine 300 when compared to non-CKD control mice (**Figure 6F**). MyoAAV-shAHR treatment significantly decreased the abundance of both the PDK4 protein and the phosphorylation of PDHE1α at serine 300 (**Figure 6F**). Using cultured muscle cells, IS and L-Kyn treatment were also found to increase *Pdk4* mRNA expression and the phosphorylation of PDHE1α at serine 300 (**Supplemental Figure 10**). To confirm transcription regulation of *Pdk4* by the AHR, we generated a transcriptionally inept CAAHR by mutating the 39$^{th}$ amino acid from arginine to aspartate (R39D) which dramatically reduces DNA binding affinity (61) (**Figure 7A**). Whereas expression of the CAAHR and R39D mutant both increase Ahr mRNA levels equally, Cyp1a1 expression was only increased in the CAAHR treated muscle cells (**Figure 7B**). *Pdk4* mRNA levels were significantly increased in muscle cells treated with the CAAHR, whereas the R39D mutant and GFP-treated muscle cells had similar *Pdk4* expression (**Figure 7C**). Compared with GFP or R39D treated muscle cells, CAAHR treated cells had significantly impaired pyruvate-supported OXPHOS (**Figure 7D**).

## DISCUSSION

A progressive skeletal myopathy has been established in patients with CKD and contributes to symptoms of exercise intolerance and lower quality of life. Whereas the pathways driving muscle wasting/atrophy in CKD have been well described (10, 62), less is understood about the metabolic insufficiency observed in skeletal muscle of these patients (4, 18, 20, 63, 64). In this study, we identified AHR activation in the skeletal muscle of patients and mice with CKD. Skeletal muscle-specific deletion of the AHR in

mice with CKD and elevated tryptophan-derived uremic metabolites significantly improved mitochondrial OXPHOS in male mice only, and these improvements were greatest when mitochondria were fueled by pyruvate rather than fatty acids. Mechanistically, AHR activation in muscle resulted in increased PDK4 expression (mRNA and protein) and subsequent phosphorylation of the PDH enzyme causing impaired enzyme activity.

CKD is a multifactorial disease which complicates investigations to understand skeletal muscle pathology. Contributing factors include metabolic acidosis, chronic inflammation, overactivation of renin angiotensin signaling, oxidative stress, and retention of uremic metabolites, often described as “toxins”. The accumulation of tryptophan-derived uremic metabolites including indoxyl sulfate, indole-3-acetic acid, L-kynurenine, and kynurenic acid have been associated with disease severity and mortality rates in CKD patients (65-68). Treatment with AST-120, an orally administered spherical carbon adsorbent that lowers indoxyl sulfate levels in systemic circulation (69), was reported to improve exercise capacity and muscle mitochondrial biogenesis in mice with CKD (70). However, in a randomized controlled trial with CKD patients, AST-120 failed to significantly improve walking speed, grip strength, muscle mass, or perceived quality of life (71). This brings to question whether other uremic metabolites are contributing to muscle pathology in CKD. Kynurenines have been associated with chronic inflammation and uremic symptoms in CKD patients (66) and mice with elevated circulating kynurenine display impaired muscle OXPHOS function (55). Notably, kynurenine and kynurenic acid levels increase significantly with respect to CKD severity and are incompletely removed from the blood by hemodialysis treatment (66). Moreover, prolonged PCr recovery in

skeletal muscle of CKD patients (a marker of in vivo mitochondrial dysfunction) was found to associate with eGFR, occurred prior to initiation of hemodialysis, and was lowest in patients receiving hemodialysis treatment (2). Thus, the progressive accumulation of uremic metabolites, especially ones that may be poorly filtered by conventional dialysis membranes, may be significant contributors to the progressive decline of mitochondrial health observed in patients with CKD.

Indoles and kynurenines are known ligands of the AHR (37, 38, 72), whose prolonged activation has been associated with the development of metabolic syndrome (44, 45), disruption of circadian rhythms (73), altered glucose and lipid metabolism (45, 74, 75), and mitochondrial respiratory impairments (76-78). To date, only three studies have investigated the role of the AHR in skeletal muscle (26, 48, 49), although previous studies have reported AHR activation in the blood of CKD patients (46, 79). In this study, skeletal muscle-specific AHR deletion improved mitochondrial OXPHOS function in CKD mice only in combination with probenecid treatment to further elevate uremic metabolites and AHR activation. However, it is important to note that several naturally occurring AHR polymorphisms occur in mice and the $AHR^{mKO}$ mice used in this study harbor a less sensitive $Ahr^{d}$ allele, as compared to the $Ahr^{b1}$ allele found in C57BL/6J mice, because they were generated using 129-SvJ embryonic stem cells (80). Thus, they have lower levels of AHR activation for a given dosage of ligand compared to the AHR allele found in C57BL/6J mice. To address this issue, we performed several experiments. First, $AHR^{mKO}$ and littermates with CKD were treated with probenecid, an organic anion transporter inhibitor that decreases the kidney's ability to eliminate uremic toxins (54). Probenecid was found in enhance serum uremic metabolite levels and muscle AHR

activation (*Cyp1a1* and *Ahrr* mRNA expression), particularly in male mice (**Figure 2**). Consequently, higher levels of AHR activation caused by treatment with probenecid revealed a significant improvement in mitochondrial OXPHOS in male mice but not female mice (**Figure 3**). Next, we performed experiments in the C57BL/6J mouse that expresses the high affinity $Ahr^{b1}$ allele by employing genetic knockdown (MyoAAV-shAHR) in CKD mice. In each of these, limiting AHR activation in CKD was found to promote improvements in mitochondrial OXPHOS with carbohydrate fuels in male but not female mice. Whether or not a progressive AHR activation occurs across increasing stages of CKD in human patients remains to be explored. However, it is intriguing that two studies in patients with CKD have reported stepwise impairment of muscle mitochondrial function with increasing CKD severity. Bittel *et al*. (81) reported that carbohydrate supported mitochondrial respiration (measured ex vivo) decreased with CKD severity. Similarly, in vivo phosphorus magnetic resonance spectroscopy analyses of muscle energetics performed by Gamboa *et al*. (82) showed a progressive increase in the time constant for phosphocreatine resynthesis (an index of lower muscle oxidative capacity) with across tertiles of eGFR. While more experimentation is necessary, these observations align with our observation that AHR activation is inversely correlated with muscle mitochondrial respiration.

While the mechanisms underlying the fact that AHR deletion and knockdown improved OXPHOS in male mice only are unknown, reports of sexual dimorphism in AHR biology have been reported. For example, differences in the response to 2,3,7,8-tetrachlorodibenzodioxin (TCDD, a potent AHR agonist) treatment have been reported in

the livers of male and female mice (83). Furthermore, it has been reported that the ligand activated AHR complex can physically associate with the estrogen receptor, as well as the androgen receptor and alter sex hormone signaling (84). AHR activation has also been shown to promote proteasomal degradation of the estrogen receptor through the cullin 4B ubiquitin ligase pathway (85) and alter sex hormone secretion (86). It is unknown if there are sex-dependent differences in AHR biology in human patients with CKD or regarding muscle mitochondrial function, although several studies investigating muscle energetics in patients with CKD have included both male and female patients and sex differences were not specifically described (4, 18, 82)

Enhanced mitochondrial OXPHOS function in male mice with AHR deletion or knockdown was present only when pyruvate was the primary fuel source. This was similar to a recent study exploring ischemic myopathy in the context of CKD (49). Additionally, C2C12 myotubes treated with uremic serum from rodents exhibited lower OXPHOS function in the presence of glucose, but not when fueled by fatty acids (87). Regarding potential mechanisms by which AHR may impair muscle mitochondrial OXPHOS, we found that PDH activity was significantly lower in both male and female mice that received AAV-CAAHR treatment. This is noteworthy because several studies have shown that uremic metabolites alone (25), as well as CKD (22), can impair matrix dehydrogenase activity. Protein and mRNA analysis of mouse muscle from both CKD animals and those with ectopic CAAHR expression confirmed that AHR activation resulted in significant increases in the expression of PDK4, a negative regulator of the PDH enzyme, as well as phosphorylation of the PDH enzyme (**Figure 6**). Further experimentation in cultured

muscle cells uncovered increased PDH phosphorylation following treatment AHR ligands IS and L-Kyn (**Supplemental Figure 10**). In support of these findings, patients with CKD have been reported to display decreased PDH activity and upregulated PDK4 expression in skeletal muscle (88). Taken together, these findings establish a uremic metabolite-Ahr-Pdk4 axis as a mechanism contributing to skeletal muscle mitochondrial OXPHOS impairment in CKD.

Incongruent with our hypothesis, deletion of the AHR in skeletal muscle did not improve muscle size or function in mice with CKD. This contrasts with our recent study on the ischemic myopathy with CKD (49). A possible explanation for lack of agreement likely stems from the hypoxic/ischemic microenvironment, especially considering that the AHR's transcriptional fidelity requires dimerization with the aryl hydrocarbon receptor nuclear translocator (ARNT), which is also known as hypoxia inducible factor 1-beta (HIF1b). The lack of improvement in muscle function or size with AHR deletion observed herein may be attributed to non-AHR dependent effects of CKD and uremic metabolites. For example, indoxyl sulfate was found to increase reactive oxygen species (ROS) production via activation of NADPH oxidases in cultured muscle cells (26). This increase in NADPH oxidase activity might initiate ROS-dependent atrophy pathways (89, 90) which are elevated in CKD muscle. Other contributing factors may include metabolic acidosis, chronic inflammation, overactivation of renin angiotensin signaling in the CKD condition which do not involve the AHR.

The current study is not without limitations. First, due to limited specimen size in muscle biopsy tissue from human participants, it was not possible to perform comprehensive assessments on skeletal muscle mitochondrial function as done in the animal models. Second, although mice used were fully mature and females were ovariectomized to better mimic the post-menopausal state of most female CKD patients (91), the mice used in this study were relatively young despite age being a significant risk factor for CKD. Because the OXPHOS assessments employed require harvesting muscle tissue, these analyses were terminal and repeated temporal assessments of mitochondrial OXPHOS were not possible. Thus, we could not establish whether the mitochondrial OXPHOS impairment (secondary to AHR activation) leads to muscle atrophy or contractile dysfunction with longer durations of AHR activation. All experiments involving rodents with CKD were performed on mice fed an adenine-supplemented diet, whereas other studies have employed surgical models of CKD (5/6 nephrectomy) (92, 93). We have shown that adenine and 5/6 nephrectomy models have similar levels of uremic metabolites, muscle atrophy, and mitochondrial dysfunction (24). Regarding uremic metabolites, it is worth noting that there may be differences in the relative abundance of AHR ligands in the adenine model compared to patients with CKD, although larger and more comprehensive quantification is necessary to fully assess these differences. Additionally, our metabolite analysis herein did not include quantification of indoles although we have previously reported their increase in mice fed adenine diet to induce CKD (22, 24). Probenecid, a drug that reduces uric acid levels and is used to treat gout, was employed to elevate uremic metabolites levels as done previously (54) with the goal of increasing muscle AHR activation. Adenine is a purine base that can be converted

to uric acid by xanthine oxidase and the combination of adenine feeding and probenecid could impact the degree of renal impairment in our experiments, although blood urea nitrogen levels were similar in CKD and CKD+probenecid mice (**Supplemental Figure 2**). The degree of kidney injury with adenine feeding may be related to uric acid levels as inhibition of xanthine oxidase attenuated kidney injury in this model (94). Nonetheless, it is important to consider any potential effects this combination could have because hyperuricemia occurs in patients with CKD and associates with mortality (95) and uric acid release occurs in atrophying muscle (96).

Collectively, the findings herein establish a tryptophan-derived uremic metabolite-AHR-Pdk4 axis as a critical regulator skeletal muscle mitochondrial function in CKD, when fueled by pyruvate, and provide evidence that interventions that disrupt this axis can improve muscle mitochondrial function.

## METHODS

**Sex as a Biological Variable**. Our study examined male and female animals, and sex-dimorphic effects are reported. Human participants included both male and female individuals (self-identified), but the sample size was not powered to detect differences in sex.

***Humans Subjects.*** Muscle specimens of the gastrocnemius were collected from adult control participants with normal kidney function and patients with CKD via percutaneous

muscle biopsy using sterile procedures (49, 97). The physical and clinical characteristics of these participants are shown in **Supplemental Table 1**. All participants in this study were free from peripheral vascular disease and distinct from our prior study on the role of the AHR in peripheral artery disease (49). Non-CKD adult controls and patients with CKD were recruited from the UF Health Shand's hospital or Malcom Randall VA Medical Center. Inclusion criteria for CKD patients included an eGFR between 15-45 mL/min/1.73*$m^2$ for at least 3 months that were not on hemodialysis. Inclusion criteria for Non-CKD adult controls was an eGFR greater than 80 mL/min/1.73*$m^2$. eGFR was calculated using the CKD-EPI Creatine equation (2021) (98). Exclusion criteria for both groups included being an active smoker (must be tobacco free for >6 months) due to tobacco smoke containing AHR ligands (99). A portion of the muscle samples was cleaned and quickly snap froze in liquid nitrogen. Another portion was immediately placed in ice-cold buffer X (50 mM K-MES, 7.23 mM $K_2$EGTA, 2.77 mM Ca$K_2$EGTA, 20 mM imidazole, 20 mM taurine, 5.7 mM ATP, 14.3 mM phosphocreatine, and 6.56 mM $MgCl_2$-$6H_2O$, pH 7.1) for preparation of permeabilized fiber bundles (97, 100). Fiber bundles were mechanically separated using needle-tipped forceps under a dissecting scope and subsequently permeabilized with saponin (30 µg/ml) for 30 minutes at 4°C on a nutating mixer, and then washed in ice-cold buffer Z (105 mM K-MES, 30 mM KCl, 1 mM EGTA, 10 mM $K_2HPO_4$, 5 mM $MgCl_2$-$6H_2O$, 0.5 mg/ml bovine serum albumin (BSA), pH 7.1) for 15 minutes until analysis. High-resolution $O_2$ consumption measurements were conducted at 37˚C in buffer Z (in mmol/l) (105 K-MES, 30 KCl, 1 EGTA, 10 $K_2HPO_4$, 5 $MgCl_2 6H_2O$, 0.5 mg/ml BSA, pH 7.1), supplemented with creatine monohydrate (5 mM), using the Oroboros O2K Oxygraph. Mitochondrial respiration was measured energizing

the bundles with 5mM pyruvate and 2.5mM malate followed by the addition of 4mM adenosine diphosphate (ADP) to stimulate maximal respiration. At the end of experiments, the bundles were retrieved, washed in distilled water, lyophilized (Labconco), and the dry weight was obtained using a Mettler Toledo MX5 microbalance. Rates of $O_2$ consumption ($JO_2$) were normalized to the bundle dry weight. All study procedures were carried out according to the Declaration of Helsinki and participants were fully informed about the research and informed consent was obtained.

***Animals.*** AHR conditional knockout mice ($AHR^{cKO}$) with loxP sites flanking exon 2 of the AHR ($AHR^{tm3.1Bra/J}$) were obtained from Jackson Laboratory (Stock #006203). $AHR^{cKO}$ mice were bred with a tamoxifen inducible skeletal muscle-specific Cre line (Tg(ACTA1-cre/Esr1*)2Kesr/J, Jackson Laboratories, Stock No. 025750) to generate skeletal muscle-specific inducible AHR knockout mice ($AHR^{mKO}$). Female mice underwent bilateral ovariectomy (OVX) 14-days prior to inducing Cre-mediated DNA recombination. Deletion of the AHR was initiated at 5-months of age by intraperitoneal (IP) injection of tamoxifen (MilliporeSigma Cat. No. T5648) for five consecutive days (120mg/kg). Littermate AHR floxed mice without the Cre transgene ($AHR^{fl/fl}$) that received the same tamoxifen dosing were used as controls. For adeno associated virus (AAV) experiments, C57BL/6J mice (Stock #000664) were obtained from The Jackson Laboratory at 5 months of age (N=60 total mice). Female mice underwent OVX 14-days prior to delivery of AAV. All rodents were housed in a temperature (22˚C) and light controlled (12-hour light/12-hour dark) room and maintained on standard chow diet (Envigo Teklad Global 18% Protein Rodent Diet 2918 irradiated pellet) with free access to food and water. All animal experiments

adhered to the *Guide for the Care and Use of Laboratory Animals* from the Institute for Laboratory Animal Research, National Research Council, Washington, D.C., National Academy Press.

***Plasmid Construction and Adeno-Associated Virus Production/Delivery***. AAV backbones were obtained from Cell Biolabs, USA (Cat. No. VPK-411-DJ). To accomplish muscle specific expression of transgenes, a human skeletal actin (*Acta1*; abbreviated as HSA) was PCR amplified from human genomic DNA from a patient's muscle biopsy. The AAV-HSA-GFP plasmid was developed by inserting the HSA promoter and GFP (ZsGreen1) into a promoter-less AAV vector (Cat. No. VPK-411-DJ; Cell BioLabs, USA) using In-Fusion Cloning (Takara Bio, USA; Cat. No. 638911). To generate a constitutively active AHR (CAAHR) vector, the mouse AHR coding sequence was PCR amplified from genomic DNA obtained from a C57BL6J mouse such that the ligand binding domain (amino acids 277–418) was deleted for the murine AHR and subsequently cloned and inserted downstream of the HSA promoter using In-Fusion cloning. The resulting plasmids were packaged using AAV2/9 serotype by Vector Biolabs (Malvern, PA). The skeletal muscle-specific AAV9's were delivered via several small volume intramuscular injections of the hindlimb muscle TA, EDL, and gastrocnemius plantar flexor complex at a dosage of 5E+11 vg/limb. To knockdown the AHR in skeletal muscle, we utilized an siRNA sequence (AHR siRNA: 5'-AAG UCG GUC UCU AUG CCG CTT-3') and a GFP control that were packaged using a mutated AAV9 capsid variant that enables muscle specific expression (MyoAAV4a) (101) by Vector Biolabs (Malvern, PA). MyoAAV's were delivered via a tail injection at a dosage of 1E+11 vg/kg. To generate a transcriptionally

deficient CAAHR mutant, we performed Q5 site-directed mutagenesis (NEB, Cat. No. E0554S) to mutant arginine-39 to aspartate (R39D) (61).

***RNA Isolation and quantitative PCR.*** Total RNA was isolated using TRIzol (Invitrogen, Cat. No. 15-596-018). All samples were homogenized using a PowerLyzer 24 (Qiagen) and RNA was isolated using Direct-zol RNA MiniPrep kit (Zymo Research, Cat. No. R2052). cDNA was generated from 500ng of RNA using the LunaScript RT Supermix kit (New England Biolabs, Cat. No. E3010L). Real-time PCR (RT-PCR) was performed on a Quantstudio 3 (ThermoFisher Scientific) using either Luna Universal qPCR master mix for Sybr Green primers (New England Biolabs, Cat. No. M3003X) or Taqman Fast Advanced Master mix (ThermoFisher Scientific, Cat. No. 4444557). All primers and Taqman probes used in this work are listed in **Supplemental Table 2**. Relative gene expression was calculated as $2^{-\Delta\Delta CT}$ from the control group.

***Muscle Cell Culture Experiments.*** C2C12 murine myoblasts were obtained from ATCC (Cat. No. CRL-1772) and grown in Dulbecco's modified Eagle's medium (DMEM, GIBCO; Cat. No. 10569) supplemented with 10% fetal bovine serum (VWR; Cat. No. 97068) and 1% penicillin streptomycin (GIBCO; Cat. No. 15140) at 37°C and 5% $CO_2$. All cell culture experiments were performed with low passage cells (passages one through five) and in at least three biologically independent lots of myoblasts. When assessing AHR activation in muscle cells, C2C12 myoblast were incubated for 6-hours with 100μM of AHR agonist indoxyl sulfate (IS), L-kyurenine (L-Kyn), kynurenic acid (KA), and indole-3-acetic acid

(IAA). Myoblast were washed with phosphate buffered saline (PBS) and collected in TRIzol reagent for total RNA isolation.

***Western Blotting.*** C2C12 muscle cells and snap frozen mouse tissue were homogenized in CelLytic M lysis buffer (MilliporeSigma, Cat. No. C2978) supplemented with protease and phosphatase inhibitors (ThermoScientific, Cat. No. A32961) in glass Teflon homogenizers and centrifuged at 10,000g for 10-minutes at 4°C. The supernatant was collected, and protein quantification was performed using a bicinchoninic acid protein assay (ThermoFisher Scientific; Cat. No. SL256970). 2x Laemmli buffer (BioRad; Cat. No. 161-0737) and β-mercaptoethanol (ACROS; Cat. No. 60-24-2) were added to the samples which were incubated in boiling water for five minutes. 10µl of a pre-stained ladder (BioRad; Cat. No. 1610394) was loaded in the first lane of a 7.5% Criterion TGX Stain-Free Protein Gel (BioRad; Cat. No. 5678023) while 20µg (cell lysate) and 100µg (tissue lysate) of each sample was loaded. Gel electrophoresis was run at 100V for 1.5 hours and then imaged for total protein on a BioRad imager (GelDoc EZ Imager), before transferring to a polyvinylidene fluoride (PVDF) membrane using a BioRad Trans Blot Turbo system. The PVDF membrane was then imaged for total protein and incubated in blocking buffer (Licor; Cat. No. 927-60001) for one-hour at room temperature while rocking. The membrane was incubated overnight at 4°C with AHR primary antibody (NSJ Bioreagents; Cat. No. R30877, 1µg/ml), PhosphoDetect Anti-PDH-E1α ($pSer^{300}$) primary antibody (Millipore-Sigma; Cat. No. AP1064, 0.2µg/ml), or PDK4 primary antibody (ProteinTech; Cat. No. 12949-1-AP, 1:1000) in blocking buffer. After overnight incubation, the membranes were washed 3x10 minutes with TBS+0.01% tween. The membranes

were then incubated for two-hours in blocking solution with secondary antibody (Licor; Cat. No. C80118-05, 1:10,000 dilution) to detect the AHR, PDH-E1α ($pSer^{300}$), and PDK4, while the total PDHE1α antibody was conjugated to AlexaFluor790 (Santa Cruz; Cat. No. 377092AF790). Next, the membranes were then washed 3x10 minutes in TBS+0.01% tween and imaged on a Licor Odyssey CLx. Uncropped blots and gel images are provided in the Supplement.

***RNA Validation of Skeletal Muscle Specific Knockout of the AHR.*** The soleus muscle was dissected from healthy $AHR^{fl/fl}$ mice and $AHR^{mKO}$ mice and incubated in Krebs buffer supplemented with 10mM glucose and gassed with 95% $O_2$ and 5% $CO_2$ at 37°C. The muscles were treated with 500μM indoxyl sulfate (IS) or equal volume of DMSO for 3.5 hours and then processed for qPCR analysis.

***Induction of Chronic Kidney Disease (CKD).*** Two weeks after tamoxifen treatment, mice were assigned to a casein-based chow diet for seven days, followed by induction of CKD via the addition of 0.2% (w/w) adenine to the diet. CKD mice were kept on 0.2% adenine diet for the duration of the study. Control mice were fed a casein-based chow diet for the entirety of the experiment.

***Delivery of Probenecid.*** Mice were administered IP injections of 25mg/kg of probenecid twice daily (Invitrogen; Cat. No. P36400) or PBS (vehicle control) starting two weeks post-CKD induction, for the duration of two weeks. On the last day of injections, probenecid or

PBS was administered two hours prior to euthanasia. Plasma was isolated and stored at -80°C for further metabolomic analyses described below.

***Targeted Metabolomics in Mouse Plasma.*** Targeted metabolomic analyses were performed by the Southeast Center for Integrated Metabolomics at the University of Florida. Under ketamine (100mg/kg) and xylazine (10mg/kg) anesthesia, blood was collected via cardiac puncture using a heparin coated syringe, centrifuged at 4,000rpm for 10 minutes, and plasma was stored at -80°C until analysis. Plasma was processed as done previously (22, 24).

***Assessment of Renal Function.*** GFR was evaluated by measuring FITC-labeled inulin clearance (102, 103). GFR was assessed via blood collection from a small ~1mm tail snip at multiple time points (3, 5, 7, 10, 15, 35, 56, 75 minutes) following retro-orbital injection of FITC-labeled inulin (MilliporeSigma; Cat. No. F3272) in heparin coated capillary tubes. Blood collected was centrifuged at 4,000rpm for 10-minutes at 4°C and plasma was diluted (1:20) and loaded into a 96-well plate along with a FITC-inulin standard curve and fluorescence was detected using a BioTek Synergy II plate reader. GFR was calculated using a two-phase exponential decay. BUN was assessed from plasma collected prior to euthanasia using a commercial kit (Arbor Assays; Cat. No. K024).

***Assessment of Forelimb Grip Strength.*** Bilateral forelimb grip strength was assessed using a grip strength meter (BIOSEB; Model No. BIO-GS3). Mice were encouraged to firmly grip the metal T-bar and were pulled backward horizontally with increasing force

588 until they released the T-bar. Three trials were performed allowing the mice 30-seconds
589 to rest between each trial and the highest force was analyzed.
590
591 ***Peroneal Nerve Stimulated EDL Force Frequency and Fatigue Analysis.*** Mice were
592 anesthetized with an IP injection of xylazine (10mg/kg) and ketamine (100mg/kg) and the
593 distal portion of the extensor digitorum longus (EDL) tendon was sutured with a double
594 square knot using 4-0 silk suture and the tendon was carefully cut distal to the suture.
595 The mouse was placed prone on a thermoregulated platform (37°C) and the knee was
596 immobilized/stabilized with a pin attached to the platform. The suture attached to the distal
597 end of the EDL tendon was secured to a force length transducer (Cambridge Technology;
598 Model: 2250), and two Chalgren electrodes (Cat. No. 111-725-24TP) were placed on both
599 sides of the peroneal nerve and connected to an Aurora Scientific stimulator (701A
600 stimulator). Data was collected using the DMC program (version v5.500, Aurora
601 Scientific). Optimal length was determined by recording force production of twitch
602 contractions while incrementally increasing muscle length with 60 seconds of rest
603 between each contraction. Once optimal length was achieved, the EDL underwent a force
604 frequency assessment by stimulating the peroneal nerve at 1, 25, 50, 75, 100, 125, 150,
605 and 175 Hz (spaced one minute apart) using 2.4 mAmp stimulation, 0.1 ms pulse width,
606 and a train duration of 0.5 s. Specific force was calculated by normalizing absolute force
607 production to the EDL mass. Following force frequency analysis, the EDL was rested for
608 two minutes, before undergoing a series of 80 contractions at 50 Hz (2.4mAmp
609 stimulation, 0.1 ms pulse width, and train duration of 0.5 s) performed every two seconds
610 to assess fatiguability of the muscle.

***Mitochondrial Isolation.*** Skeletal muscle mitochondria were isolated from the gastrocnemius and quadriceps muscles. Dissected muscles were immediately placed in ice-cold Buffer A (phosphate buffered saline supplemented with EDTA (10mM), pH=7.4), and trimmed to remove connective tissue and fat before it was minced and subjected to a five-minute incubation on ice in Buffer A supplemented with 0.025% trypsin (Millipore Sigma; Cat. No. T4799). Following trypsin digestion, skeletal muscle was centrifuged at 500g for five minutes and the supernatant was aspirated to remove trypsin. Digested muscle tissue was resuspended in Buffer C (MOPS (50mM), KCl (100mM), EGTA (1mM), $MgSO_4$ (5mM), bovine serum albumin (BSA; 2g/L); pH=7.1) and homogenized via a glass-Teflon homogenizer (Wheaton) for ~five-passes and subsequently centrifuged at 800g for 10 minutes. The resulting supernatant was collected in a separate tube and centrifuged at 10,000g for 10-minutes to pellet mitochondria. All steps were performed at 4°C. The mitochondrial pellet was gently washed with Buffer B (MOPS (50mM), KCl (100mM), EGTA (1mM), $MgSO_4$ (5mM); pH=7.1) to remove damaged mitochondria on the exterior of the pellet and then re-suspended in Buffer B. Protein concentration was determined using a bicinchoninic acid protein assay (ThermoFisher Scientific; Cat. No. A53225).

***Skeletal Muscle Mitochondrial OXPHOS Function.*** High resolution respirometry was measured using Oroboros Oxygraph-2k (O2K) measuring oxygen consumption ($JO_2$) at 37°C in Buffer D (105mM K-MES, 30mM KCl, 1mM EGTA, 10mM $K_2HPO_4$, 5mM $MgCl_2$-$6H_2O$, 2.5mg/ml BSA, pH 7.2) supplemented with 5mM creatine (Cr). A creatine kinase

(CK) clamp was employed to leverage the enzymatic activity of CK, which couples the interconversion of ATP and ADP to that of phosphocreatine (PCr) and free Cr, to titrate the extra mitochondrial ATP/ADP ratio, thus the free energy of ATP hydrolysis ($\Delta G_{ATP}$) could be calculated(104). This approach allows assessment of mitochondrial flux across a range of physiological relevant energetic demands ($\Delta G_{ATP}$, heavy exercise to rest) which are controlled by altering the PCr/Cr ratio. The $\Delta G_{ATP}$ can be plotted against the corresponding $JO_2$ creating a linear force-flow relationship, where the slope represents the conductance through the OXPHOS system. 25µg of mitochondria were added to the Oxygraph chamber in two milliliters of Buffer D supplemented with ATP (5mM), Cr (5mM), PCr (1mM), and CK (20U/mL) at 37°C. Conductance measurements were performed using various combinations the following substrates: pyruvate (5mM), malate (2.5mM), and octanoyl-L-carnitine (0.2mM). In all experiments, exogenous cytochrome c was added to confirm the outer mitochondrial membrane was intact.

***JNAD(P)H Matrix Dehydrogenase Assays.*** Matrix dehydrogenase function was assessed utilizing the autofluorescence of NADH or NADPH (Ex/Em = 340/450) in a 96-well plate using a kinetic protocol on a BioTek syergy 2 multimode Microplate Reader. For all assays, Buffer D was supplemented with alamethicin (0.03 mg/mL), rotenone (0.005 mM), NAD+ or NADP+ (2 mM). Dehydrogenase enzymes such as pyruvate dehydrogenase (PDH) and alpha ketoglutarate dehydrogenase (AKGDH) required supplementation of cofactors Coenzyme A (0.1 mM), and thiamine pyrophosphate (0.3 mM, TPP). Pre-warmed Buffer D (37°C) was loaded in a 96-well plate followed by the addition of mitochondria. Dehydrogenase activity was initiated with the addition of

enzyme-specific fuel sources: pyruvate (5mM, PDH), glutamate (10mM, glutamate dehydrogenase (GDH)), malate (5mM, malate dehydrogenase (MDH) and malic enzyme (ME)), alpha ketoglutarate (10 mM, AKGDH), citrate (6 mM, aconitase), fumarate (10 mM, fumarate hydratase (FH)), hydroxybutyrate (10 mM, beta hydroxy butyrate dehydrogenase (βHBDH)), or isocitrate (5 mM, isocitrate dehydrogenase 2 and 3 (ICDH2/3)). Rates of NADH/NADPH production was calculated as a slope of linear portions of NADH/NADPH curves and converted to pmols of NADH/NADPH by a standard curve.

***Complex V Activity (ATP Synthase).*** Mitochondria were lysed in Cell Lytic M and enzyme activity was measured in Buffer E (2.5mM $MgCl_2$-$6H_2O$, 20mM HEPES, 100mM KCl, 2.5mM $KH_2PO_4$, 1% glycerol, pH=8.0) supplemented with lactate dehydrogenase (10mM), pyruvate kinase (10mM), rotenone (0.005mM), phospho-enol-pyruvate (PEP, 5mM), and NADH (0.2mM). In this assay, the ATP synthase works in reverse (hydrolysis of ATP) as the mitochondrial membrane potential was dissipated by lysis. Using a pyruvate kinase/lactate dehydrogenase coupled assay, ATP hydrolysis (by the ATP synthase) is coupled to NADH consumption in a 1:1 stoichiometry. The rate of decay of NADH autofluorescence (Ex/Em = 340/450 nm) represents ATP synthase activity. Fluorescence values were converted to pmols of NADH by a standard curve.

***Immunofluorescence Microscopy.*** 10μm-thick transverse sections were cut from the tibialis anterior, extensor digitorum longus, and soleus muscles mounted in optimal cutting temperature compound and frozen in liquid nitrogen-cooled isopentane using a Leica

3050S cryotome. Muscle sections were fixed with 4% paraformaldehyde in PBS for five minutes at room temperature followed by ten minutes of permeabilization using 0.25% (v/v) Triton X-100 in PBS. Next, sections were washed with PBS three times for 2-minutes each wash. Sections were blocked for one-hour at room temperature with blocking buffer (PBS supplemented with 5% goat serum and 1% BSA). Sections were incubated overnight at 4°C with a primary antibody against laminin (1:100 dilution, Millipore Sigma; Cat. No. L9393) to label myofiber membranes. Following four PBS washes, sections were incubated for one-hour with Alexa-Fluor secondary antibodies (ThermoFisher Scientific, 1:100 dilution), and then was four times (five minutes each) and coverslips were mounted with Vectashield hardmount containing DAPI (Vector Laboratories; Cat. No. H1500) to label nuclei. Muscle sections were imaged at 20x magnification using an Evos FL2 Auto microscope. All images were analyzed for CSA using MuscleJ (105).

**ATAC Sequencing**. Nuclei were isolated by gentle homogenization (10 mM Tris-HCl (pH 7.5), 10 mM NaCl, 3 mM MgCl2, 0.1% Tween-20, 0.1% NP-40, and 0.01% Digitonin) of skeletal muscle followed by tagmentation (Tagment DNA buffer and Tn5, Illumina) for 30 minutes at 37C. DNA was then purified with the MinElute purification kit from Qiagen. The purified DNA was PCR amplified for 15 cycles using Q5 High Fidelity DNA polymerase (New England Biolabs, M0491S) with the incorporation of Illumina Nextera XT adaptors (Illumina). The libraries were then size selected with AmpureXP Beads (Beckman, Cat# A63880). Quality control of the libraries was verified using a bioanalyzer. Libraries were sequenced on Illumina HiSeq4000 using Paired End (PE) 150 bp. The reads were first mapped to the GRCm39-mm39 mouse genome assembly using Bowtie2 version 2.1.0.

Mitochondrial, duplicate, and non-unique reads were removed before peak calling. MACS2 was used for peak calling employing BAMPE mode. Differentially expressed peaks were identified using edgeR.

**Statistical Analysis.** Data are presented as the mean ± SD. Normality of data was assessed using the Shapiro-Wilk test. Data without normal distribution were analyzed using a Kruskal-Wallis test. Data involving comparisons of two groups were analyzed using a two-tailed Student's *t*-test. Data involving comparisons of more than two groups were analyzed using either a one-way ANOVA with Tukey's post hoc or a two-way ANOVA with Dunnett's post hoc testing for multiple comparisons when significant interactions were detected. Pearson correlations involved two-tailed statistical testing. All analyses were performed in GraphPad Prism (Version 9.5.1). $P<0.05$ was considered significant.

**Study Approval.** All human experiments in this study were approved by the institutional review boards (Protocol IRB201801553) at the University of Florida and the Malcom Randall VA Medical Center (Gainesville, FL). All animal experiments in this study were approved by the Institutional Animal Care and Use Committee of the University of Florida (Protocol 202110484).

**Data Availability.** A single XLS file that provides all data in the manuscript and supplement has been made available with this publication. Raw sequencing data have been uploaded to the Gene Expression Omnibus (Accession Number GSE255812).

**Acknowledgements:** This study was supported by National Institutes of Health (NIH) grant R01-HL149704 (T.E.R.). S.T.S was supported by NIH grant R01HL148597. T.T. was support by NIH grant F31-DK128920. K.W. was supported by NIH grant T32-AG062728.

**Author Contributions:** TT and TER designed the study; TT, NAV, LES, KW, STS, and TER conducted experiments. TT, NAV, LES, KW, and TER analyzed data. TT, NAV, LES, KW, STS, and TER interpreted the data. TT and TER drafted the manuscript. TT, NAV, LES, KW, STS, and TER edited and revised the manuscript. All authors approved the final version of this manuscript.

## CITATIONS

1. Collaborators GBoDS. Global, regional, and national incidence, prevalence, and years lived with disability for 301 acute and chronic diseases and injuries in 188 countries, 1990-2013: a systematic analysis for the Global Burden of Disease Study 2013. *Lancet.* 2015;386(9995):743-800.
2. Gamboa JL, Roshanravan B, Towse T, Keller CA, Falck AM, Yu C, et al. Skeletal Muscle Mitochondrial Dysfunction Is Present in Patients with CKD before Initiation of Maintenance Hemodialysis. *Clin J Am Soc Nephrol.* 2020;15(7):926-36.
3. Gregg LP, Bossola M, Ostrosky-Frid M, and Hedayati SS. Fatigue in CKD: Epidemiology, Pathophysiology, and Treatment. *Clin J Am Soc Nephrol.* 2021;16(9):1445-55.
4. Kestenbaum B, Gamboa J, Liu S, Ali AS, Shankland E, Jue T, et al. Impaired skeletal muscle mitochondrial bioenergetics and physical performance in chronic kidney disease. *JCI Insight.* 2020;5(5).
5. Mori K. Maintenance of Skeletal Muscle to Counteract Sarcopenia in Patients with Advanced Chronic Kidney Disease and Especially Those Undergoing Hemodialysis. *Nutrients.* 2021;13(5).
6. Wang XH, Du J, Klein JD, Bailey JL, and Mitch WE. Exercise ameliorates chronic kidney disease-induced defects in muscle protein metabolism and progenitor cell function. *Kidney Int.* 2009;76(7):751-9.

7. Wang X, Hu Z, Hu J, Du J, and Mitch WE. Insulin resistance accelerates muscle protein degradation: Activation of the ubiquitin-proteasome pathway by defects in muscle cell signaling. *Endocrinology.* 2006;147(9):4160-8.
8. Mitch WE. Malnutrition is an unusual cause of decreased muscle mass in chronic kidney disease. *J Ren Nutr.* 2007;17(1):66-9.
9. May RC, Kelly RA, and Mitch WE. Mechanisms for defects in muscle protein metabolism in rats with chronic uremia. Influence of metabolic acidosis. *J Clin Invest.* 1987;79(4):1099-103.
10. Wang XH, and Mitch WE. Mechanisms of muscle wasting in chronic kidney disease. *Nat Rev Nephrol.* 2014;10(9):504-16.
11. Thomas SS, and Mitch WE. Mechanisms stimulating muscle wasting in chronic kidney disease: the roles of the ubiquitin-proteasome system and myostatin. *Clin Exp Nephrol.* 2013;17(2):174-82.
12. Wang XH, and Mitch WE. Muscle wasting from kidney failure-a model for catabolic conditions. *Int J Biochem Cell Biol.* 2013;45(10):2230-8.
13. Price SR, Bailey JL, Wang X, Jurkovitz C, England BK, Ding X, et al. Muscle wasting in insulinopenic rats results from activation of the ATP-dependent, ubiquitin-proteasome proteolytic pathway by a mechanism including gene transcription. *J Clin Invest.* 1996;98(8):1703-8.
14. Zhang L, Rajan V, Lin E, Hu Z, Han HQ, Zhou X, et al. Pharmacological inhibition of myostatin suppresses systemic inflammation and muscle atrophy in mice with chronic kidney disease. *FASEB J.* 2011;25(5):1653-63.
15. Mitch WE. Proteolytic mechanisms, not malnutrition, cause loss of muscle mass in kidney failure. *J Ren Nutr.* 2006;16(3):208-11.
16. Durozard D, Pimmel P, Baretto S, Caillette A, Labeeuw M, Baverel G, et al. 31P NMR spectroscopy investigation of muscle metabolism in hemodialysis patients. *Kidney Int.* 1993;43(4):885-92.
17. Thompson CH, Kemp GJ, Taylor DJ, Ledingham JG, Radda GK, and Rajagopalan B. Effect of chronic uraemia on skeletal muscle metabolism in man. *Nephrol Dial Transplant.* 1993;8(3):218-22.
18. Roshanravan B, Kestenbaum B, Gamboa J, Jubrias SA, Ayers E, Curtin L, et al. CKD and Muscle Mitochondrial Energetics. *Am J Kidney Dis.* 2016;68(4):658-9.
19. Roshanravan B, Gamboa J, and Wilund K. Exercise and CKD: Skeletal Muscle Dysfunction and Practical Application of Exercise to Prevent and Treat Physical Impairments in CKD. *Am J Kidney Dis.* 2017;69(6):837-52.
20. Gamboa JL, Billings FT, Bojanowski MT, Gilliam LA, Yu C, Roshanravan B, et al. Mitochondrial dysfunction and oxidative stress in patients with chronic kidney disease. *Physiol Rep.* 2016;4(9).
21. Chalupsky M, Goodson DA, Gamboa JL, and Roshanravan B. New insights into muscle function in chronic kidney disease and metabolic acidosis. *Curr Opin Nephrol Hypertens.* 2021;30(3):369-76.
22. Thome T, Kumar RA, Burke SK, Khattri RB, Salyers ZR, Kelley RC, et al. Impaired muscle mitochondrial energetics is associated with uremic metabolite accumulation in chronic kidney disease. *Jci Insight.* 2021;6(1).

23. Thome T, Coleman MD, and Ryan TE. Mitochondrial Bioenergetic and Proteomic Phenotyping Reveals Organ-Specific Consequences of Chronic Kidney Disease in Mice. *Cells.* 2021;10(12).
24. Kim K, Anderson EM, Thome T, Lu GY, Salyers ZR, Cort TA, et al. Skeletal myopathy in CKD: a comparison of adenine-induced nephropathy and 5/6 nephrectomy models in mice. *Am J Physiol-Renal.* 2021;321(1):F106-F19.
25. Thome T, Salyers ZR, Kumar RA, Hahn D, Berru FN, Ferreira LF, et al. Uremic metabolites impair skeletal muscle mitochondrial energetics through disruption of the electron transport system and matrix dehydrogenase activity. *Am J Physiol Cell Physiol.* 2019;317(4):C701-C13.
26. Enoki Y, Watanabe H, Arake R, Sugimoto R, Imafuku T, Tominaga Y, et al. Indoxyl sulfate potentiates skeletal muscle atrophy by inducing the oxidative stress-mediated expression of myostatin and atrogin-1. *Sci Rep.* 2016;6:32084.
27. Enoki Y, Watanabe H, Arake R, Fujimura R, Ishiodori K, Imafuku T, et al. Potential therapeutic interventions for chronic kidney disease-associated sarcopenia via indoxyl sulfate-induced mitochondrial dysfunction. *J Cachexia Sarcopenia Muscle.* 2017;8(5):735-47.
28. Yazdi PG, Moradi H, Yang JY, Wang PH, and Vaziri ND. Skeletal muscle mitochondrial depletion and dysfunction in chronic kidney disease. *Int J Clin Exp Med.* 2013;6(7):532-9.
29. Graboski AL, and Redinbo MR. Gut-Derived Protein-Bound Uremic Toxins. *Toxins (Basel).* 2020;12(9).
30. Jourde-Chiche N, and Burtey S. Accumulation of protein-bound uremic toxins: the kidney remains the leading culprit in the gut-liver-kidney axis. *Kidney Int.* 2020;97(6):1102-4.
31. Vanholder R, De Smet R, Glorieux G, Argilés A, Baurmeister U, Brunet P, et al. Review on uremic toxins: classification, concentration, and interindividual variability. *Kidney Int.* 2003;63(5):1934-43.
32. Iitaka M, Kawasaki S, Sakurai S, Hara Y, Kuriyama R, Yamanaka K, et al. Serum substances that interfere with thyroid hormone assays in patients with chronic renal failure. *Clin Endocrinol (Oxf).* 1998;48(6):739-46.
33. Sato E, Mori T, Mishima E, Suzuki A, Sugawara S, Kurasawa N, et al. Metabolic alterations by indoxyl sulfate in skeletal muscle induce uremic sarcopenia in chronic kidney disease. *Sci Rep.* 2016;6:36618.
34. Jang IY, Park JH, Kim JH, Lee S, Lee E, Lee JY, et al. The association of circulating kynurenine, a tryptophan metabolite, with frailty in older adults. *Aging-Us.* 2020;12(21):22253-65.
35. Westbrook R, Chung T, Lovett J, Ward C, Joca H, Yang HL, et al. Kynurenines link chronic inflammation to functional decline and physical frailty. *Jci Insight.* 2020;5(16).
36. Saito K, Fujigaki S, Heyes MP, Shibata K, Takemura M, Fujii H, et al. Mechanism of increases in L-kynurenine and quinolinic acid in renal insufficiency. *Am J Physiol Renal Physiol.* 2000;279(3):F565-72.
37. Schroeder JC, Dinatale BC, Murray IA, Flaveny CA, Liu Q, Laurenzana EM, et al. The uremic toxin 3-indoxyl sulfate is a potent endogenous agonist for the human aryl hydrocarbon receptor. *Biochemistry.* 2010;49(2):393-400.

38. Denison MS, and Nagy SR. Activation of the aryl hydrocarbon receptor by structurally diverse exogenous and endogenous chemicals. *Annu Rev Pharmacol Toxicol.* 2003;43:309-34.
39. Rothhammer V, and Quintana FJ. The aryl hydrocarbon receptor: an environmental sensor integrating immune responses in health and disease. *Nat Rev Immunol.* 2019;19(3):184-97.
40. Avilla MN, Malecki KMC, Hahn ME, Wilson RH, and Bradfield CA. The Ah Receptor: Adaptive Metabolism, Ligand Diversity, and the Xenokine Model. *Chem Res Toxicol.* 2020;33(4):860-79.
41. Stevens EA, Mezrich JD, and Bradfield CA. The aryl hydrocarbon receptor: a perspective on potential roles in the immune system. *Immunology.* 2009;127(3):299-311.
42. Sato S, Shirakawa H, Tomita S, Ohsaki Y, Haketa K, Tooi O, et al. Low-dose dioxins alter gene expression related to cholesterol biosynthesis, lipogenesis, and glucose metabolism through the aryl hydrocarbon receptor-mediated pathway in mouse liver. *Toxicol Appl Pharmacol.* 2008;229(1):10-9.
43. Lee JH, Wada T, Febbraio M, He J, Matsubara T, Lee MJ, et al. A novel role for the dioxin receptor in fatty acid metabolism and hepatic steatosis. *Gastroenterology.* 2010;139(2):653-63.
44. Wang C, Xu CX, Krager SL, Bottum KM, Liao DF, and Tischkau SA. Aryl hydrocarbon receptor deficiency enhances insulin sensitivity and reduces PPAR-α pathway activity in mice. *Environ Health Perspect.* 2011;119(12):1739-44.
45. Warner M, Mocarelli P, Brambilla P, Wesselink A, Samuels S, Signorini S, et al. Diabetes, metabolic syndrome, and obesity in relation to serum dioxin concentrations: the Seveso women's health study. *Environ Health Perspect.* 2013;121(8):906-11.
46. Dou L, Poitevin S, Sallee M, Addi T, Gondouin B, McKay N, et al. Aryl hydrocarbon receptor is activated in patients and mice with chronic kidney disease. *Kidney Int.* 2018;93(4):986-99.
47. Walker JA, Richards S, Belghasem ME, Arinze N, Yoo SB, Tashjian JY, et al. Temporal and tissue-specific activation of aryl hydrocarbon receptor in discrete mouse models of kidney disease. *Kidney Int.* 2020;97(3):538-50.
48. Thome T, Miguez K, Willms AJ, Burke SK, Chandran V, de Souza AR, et al. Chronic aryl hydrocarbon receptor activity phenocopies smoking-induced skeletal muscle impairment. *J Cachexia Sarcopenia Muscle.* 2022;13(1):589-604.
49. Balestrieri N, Palzkill V, Pass C, Tan J, Salyers ZR, Moparthy C, et al. Activation of the Aryl Hydrocarbon Receptor in Muscle Exacerbates Ischemic Pathology in Chronic Kidney Disease. *Circulation research.* 2023;133(2):158-76.
50. Duranton F, Cohen G, De Smet R, Rodriguez M, Jankowski J, Vanholder R, et al. Normal and pathologic concentrations of uremic toxins. *J Am Soc Nephrol.* 2012;23(7):1258-70.
51. Vanholder R, Schepers E, Pletinck A, Neirynck N, and Glorieux G. An update on protein-bound uremic retention solutes. *J Ren Nutr.* 2012;22(1):90-4.
52. Swan JS, Kragten EY, and Veening H. Liquid-chromatographic study of fluorescent materials in uremic fluids. *Clin Chem.* 1983;29(6):1082-4.
53. Niwa T, and Ise M. Indoxyl sulfate, a circulating uremic toxin, stimulates the progression of glomerular sclerosis. *J Lab Clin Med.* 1994;124(1):96-104.

54. Bush KT, Singh P, and Nigam SK. Gut-derived uremic toxin handling in vivo requires OAT-mediated tubular secretion in chronic kidney disease. *Jci Insight.* 2020;5(7).
55. Palzkill VR, Thome T, Murillo AL, Khattri RB, and Ryan TE. Increasing plasma L-kynurenine impairs mitochondrial oxidative phosphorylation prior to the development of atrophy in murine skeletal muscle: A pilot study. *Frontiers in physiology.* 2022;13.
56. Wilson RH, and Bradfield CA. Rodent genetic models of Ah receptor signaling. *Drug Metab Rev.* 2021;53(3):350-74.
57. Niwa A, Kumaki K, Nebert DW, and Poland AP. Genetic expression of aryl hydrocarbon hydroxylase activity in the mouse. Distinction between the "responsive" homozygote and heterozygote at the Ah locus. *Arch Biochem Biophys.* 1975;166(2):559-64.
58. Poland A, Glover E, and Kende AS. Stereospecific, high affinity binding of 2,3,7,8-tetrachlorodibenzo-p-dioxin by hepatic cytosol. Evidence that the binding species is receptor for induction of aryl hydrocarbon hydroxylase. *J Biol Chem.* 1976;251(16):4936-46.
59. Tabebordbar M, Lagerborg KA, Stanton A, King EM, Ye S, Tellez L, et al. Directed evolution of a family of AAV capsid variants enabling potent muscle-directed gene delivery across species. *Cell.* 2021;184(19):4919-38.e22.
60. Andersson P, McGuire J, Rubio C, Gradin K, Whitelaw ML, Pettersson S, et al. A constitutively active dioxin/aryl hydrocarbon receptor induces stomach tumors. *Proc Natl Acad Sci U S A.* 2002;99(15):9990-5.
61. Seok SH, Lee W, Jiang L, Molugu K, Zheng A, Li Y, et al. Structural hierarchy controlling dimerization and target DNA recognition in the AHR transcriptional complex. *Proc Natl Acad Sci U S A.* 2017;114(21):5431-6.
62. Wang XH, Mitch WE, and Price SR. Pathophysiological mechanisms leading to muscle loss in chronic kidney disease. *Nat Rev Nephrol.* 2022;18(3):138-52.
63. Watson EL, Baker LA, Wilkinson TJ, Gould DW, Graham-Brown MPM, Major RW, et al. Reductions in skeletal muscle mitochondrial mass are not restored following exercise training in patients with chronic kidney disease. *Faseb J.* 2020;34(1):1755-67.
64. Thome T, Kim K, Dong G, and Ryan TE. The Role of Mitochondrial and Redox Alterations in the Skeletal Myopathy Associated with Chronic Kidney Disease. *Antioxidants & redox signaling.* 2023;38(4-6):318-37.
65. Barreto FC, Barreto DV, Liabeuf S, Meert N, Glorieux G, Temmar M, et al. Serum indoxyl sulfate is associated with vascular disease and mortality in chronic kidney disease patients. *Clin J Am Soc Nephrol.* 2009;4(10):1551-8.
66. Schefold JC, Zeden JP, Fotopoulou C, von Haehling S, Pschowski R, Hasper D, et al. Increased indoleamine 2,3-dioxygenase (IDO) activity and elevated serum levels of tryptophan catabolites in patients with chronic kidney disease: a possible link between chronic inflammation and uraemic symptoms. *Nephrol Dial Transplant.* 2009;24(6):1901-8.
67. Cheng Y, Li Y, Benkowitz P, Lamina C, Köttgen A, and Sekula P. The relationship between blood metabolites of the tryptophan pathway and kidney function: a bidirectional Mendelian randomization analysis. *Sci Rep.* 2020;10(1):12675.

68. Bao YS, Ji Y, Zhao SL, Ma LL, Xie RJ, and Na SP. Serum levels and activity of indoleamine2,3-dioxygenase and tryptophanyl-tRNA synthetase and their association with disease severity in patients with chronic kidney disease. *Biomarkers.* 2013;18(5):379-85.
69. Niwa T, Yazawa T, Ise M, Sugano M, Kodama T, Uehara Y, et al. Inhibitory effect of oral sorbent on accumulation of albumin-bound indoxyl sulfate in serum of experimental uremic rats. *Nephron.* 1991;57(1):84-8.
70. Nishikawa M, Ishimori N, Takada S, Saito A, Kadoguchi T, Furihata T, et al. AST-120 ameliorates lowered exercise capacity and mitochondrial biogenesis in the skeletal muscle from mice with chronic kidney disease via reducing oxidative stress. *Nephrol Dial Transplant.* 2015;30(6):934-42.
71. Cha RH, Kang SH, Han MY, An WS, Kim SH, and Kim JC. Effects of AST-120 on muscle health and quality of life in chronic kidney disease patients: results of RECOVERY study. *J Cachexia Sarcopenia Muscle.* 2022;13(1):397-408.
72. Kou Z, and Dai W. Aryl hydrocarbon receptor: Its roles in physiology. *Biochem Pharmacol.* 2021;185:114428.
73. Anderson G, Beischlag TV, Vinciguerra M, and Mazzoccoli G. The circadian clock circuitry and the AHR signaling pathway in physiology and pathology. *Biochem Pharmacol.* 2013;85(10):1405-16.
74. Dalton TP, Kerzee JK, Wang B, Miller M, Dieter MZ, Lorenz JN, et al. Dioxin exposure is an environmental risk factor for ischemic heart disease. *Cardiovasc Toxicol.* 2001;1(4):285-98.
75. Bock KW. Functions of aryl hydrocarbon receptor (AHR) and CD38 in NAD metabolism and nonalcoholic steatohepatitis (NASH). *Biochem Pharmacol.* 2019;169:113620.
76. Ghosh J, Chowdhury AR, Srinivasan S, Chattopadhyay M, Bose M, Bhattacharya S, et al. Cigarette Smoke Toxins-Induced Mitochondrial Dysfunction and Pancreatitis Involves Aryl Hydrocarbon Receptor Mediated Cyp1 Gene Expression: Protective Effects of Resveratrol. *Toxicol Sci.* 2018;166(2):428-40.
77. Huang Y, Zhang J, Tao Y, Ji C, Aniagu S, Jiang Y, et al. AHR/ROS-mediated mitochondria apoptosis contributes to benzo[a]pyrene-induced heart defects and the protective effects of resveratrol. *Toxicology.* 2021;462:152965.
78. Heo MJ, Suh JH, Lee SH, Poulsen KL, An YA, Moorthy B, et al. Aryl hydrocarbon receptor maintains hepatic mitochondrial homeostasis in mice. *Mol Metab.* 2023;72:101717.
79. Kolachalama VB, Shashar M, Alousi F, Shivanna S, Rijal K, Belghasem ME, et al. Uremic Solute-Aryl Hydrocarbon Receptor-Tissue Factor Axis Associates with Thrombosis after Vascular Injury in Humans. *Journal of the American Society of Nephrology.* 2018;29(3):1063-72.
80. Wilson RH, Carney PR, Glover E, Parrott JC, Rojas BL, Moran SM, et al. Generation of an Allelic Series at the Ahr Locus Using an Edited Recombinant Approach. *Toxicological Sciences.* 2021;180(2):239-51.
81. Bittel DC, Bittel AJ, Varadhachary AS, Pietka T, and Sinacore DR. Deficits in the Skeletal Muscle Transcriptome and Mitochondrial Coupling in Progressive Diabetes-Induced CKD Relate to Functional Decline. *Diabetes.* 2021;70(5):1130-44.

82. Gamboa JL, Roshanravan B, Towse T, Keller CA, Falck AM, Yu C, et al. Skeletal Muscle Mitochondrial Dysfunction Is Present in Patients with CKD before Initiation of Maintenance Hemodialysis. *Clin J Am Soc Nephro.* 2020;15(7):926-36.
83. Lee J, Prokopec SD, Watson JD, Sun RX, Pohjanvirta R, and Boutros PC. Male and female mice show significant differences in hepatic transcriptomic response to 2,3,7,8-tetrachlorodibenzo-p-dioxin. *BMC Genomics.* 2015;16(1):625.
84. Ohtake F, Baba A, Fujii-Kuriyama Y, and Kato S. Intrinsic AhR function underlies cross-talk of dioxins with sex hormone signalings. *Biochem Biophys Res Commun.* 2008;370(4):541-6.
85. Ohtake F, Baba A, Takada I, Okada M, Iwasaki K, Miki H, et al. Dioxin receptor is a ligand-dependent E3 ubiquitin ligase. *Nature.* 2007;446(7135):562-6.
86. Karman BN, Basavarajappa MS, Craig ZR, and Flaws JA. 2,3,7,8-Tetrachlorodibenzo-p-dioxin activates the aryl hydrocarbon receptor and alters sex steroid hormone secretion without affecting growth of mouse antral follicles in vitro. *Toxicol Appl Pharmacol.* 2012;261(1):88-96.
87. Serrano E, Whitaker-Menezes D, Lin Z, Roche M, and Martinez Cantarin MP. Uremic Myopathy and Mitochondrial Dysfunction in Kidney Disease. *Int J Mol Sci.* 2022;23(21).
88. Xu C, Kasimumali A, Guo X, Lu R, Xie K, Zhu M, et al. Reduction of mitochondria and up regulation of pyruvate dehydrogenase kinase 4 of skeletal muscle in patients with chronic kidney disease. *Nephrology (Carlton).* 2020;25(3):230-8.
89. Dodd SL, Gagnon BJ, Senf SM, Hain BA, and Judge AR. ROS-Mediated Activation of NF-kappa B and FOXO Dduring Muscle Disuse. *Muscle Nerve.* 2010;41(1):110-3.
90. Powers SK, Morton AB, Ahn B, and Smuder AJ. Redox control of skeletal muscle atrophy. *Free Radical Bio Med.* 2016;98:208-17.
91. Vellanki K, and Hou S. Menopause in CKD. *Am J Kidney Dis.* 2018;71(5):710-9.
92. Bailey JL, Zheng B, Hu Z, Price SR, and Mitch WE. Chronic kidney disease causes defects in signaling through the insulin receptor substrate/phosphatidylinositol 3-kinase/Akt pathway: implications for muscle atrophy. *Journal of the American Society of Nephrology : JASN.* 2006;17(5):1388-94.
93. Zhang L, Wang XH, Wang H, Du J, and Mitch WE. Satellite cell dysfunction and impaired IGF-1 signaling cause CKD-induced muscle atrophy. *Journal of the American Society of Nephrology : JASN.* 2010;21(3):419-27.
94. Diwan V, Mistry A, Gobe G, and Brown L. Adenine-induced chronic kidney and cardiovascular damage in rats. *J Pharmacol Toxicol Methods.* 2013;68(2):197-207.
95. Xia X, Luo Q, Li B, Lin Z, Yu X, and Huang F. Serum uric acid and mortality in chronic kidney disease: A systematic review and meta-analysis. *Metabolism.* 2016;65(9):1326-41.
96. Miller SG, Matias C, Hafen PS, Law AS, Witczak CA, and Brault JJ. Uric acid formation is driven by crosstalk between skeletal muscle and other cell types. *JCI Insight.* 2023.
97. Ryan TE, Kim K, Scali ST, Berceli SA, Thome T, Salyers ZR, et al. Interventional- and amputation-stage muscle proteomes in the chronically threatened ischemic limb. *Clinical and Translational Medicine.* 2022;12(1):e658.
98. Inker LA, Eneanya ND, Coresh J, Tighiouart H, Wang D, Sang YY, et al. New Creatinine- and Cystatin C-Based Equations to Estimate GFR without Race. *New Engl J Med.* 2021;385(19):1737-49.

99. Thome T, Miguez K, Willms A, Burke SK, Chandran V, de Souza AR, et al. Chronic aryl hydrocarbon receptor activity phenocopies smoking-induced skeletal muscle impairment. *J Cachexia Sarcopeni.* 2021.
100. Ryan TE, Yamaguchi DJ, Schmidt CA, Zeczycki TN, Shaikh SR, Brophy P, et al. Extensive skeletal muscle cell mitochondriopathy distinguishes critical limb ischemia patients from claudicants. *JCI Insight.* 2018;3(21).
101. Tabebordbar M, Lagerborg KA, Stanton A, King EM, Ye S, Tellez L, et al. Directed evolution of a family of AAV capsid variants enabling potent muscle-directed gene delivery across species. *Cell.* 2021;184(19):4919-+.
102. Qi Z, Whitt I, Mehta A, Jin J, Zhao M, Harris RC, et al. Serial determination of glomerular filtration rate in conscious mice using FITC-inulin clearance. *American journal of physiology Renal physiology.* 2004;286(3):F590-6.
103. Rieg T. A High-throughput method for measurement of glomerular filtration rate in conscious mice. *J Vis Exp.* 2013(75):e50330.
104. Fisher-Wellman KH, Davidson MT, Narowski TM, Lin CT, Koves TR, and Muoio DM. Mitochondrial Diagnostics: A Multiplexed Assay Platform for Comprehensive Assessment of Mitochondrial Energy Fluxes. *Cell reports.* 2018;24(13):3593-606 e10.
105. Mayeuf-Louchart A, Hardy D, Thorel Q, Roux P, Gueniot L, Briand D, et al. MuscleJ: a high-content analysis method to study skeletal muscle with a new Fiji tool. *Skelet Muscle.* 2018;8(1):25.

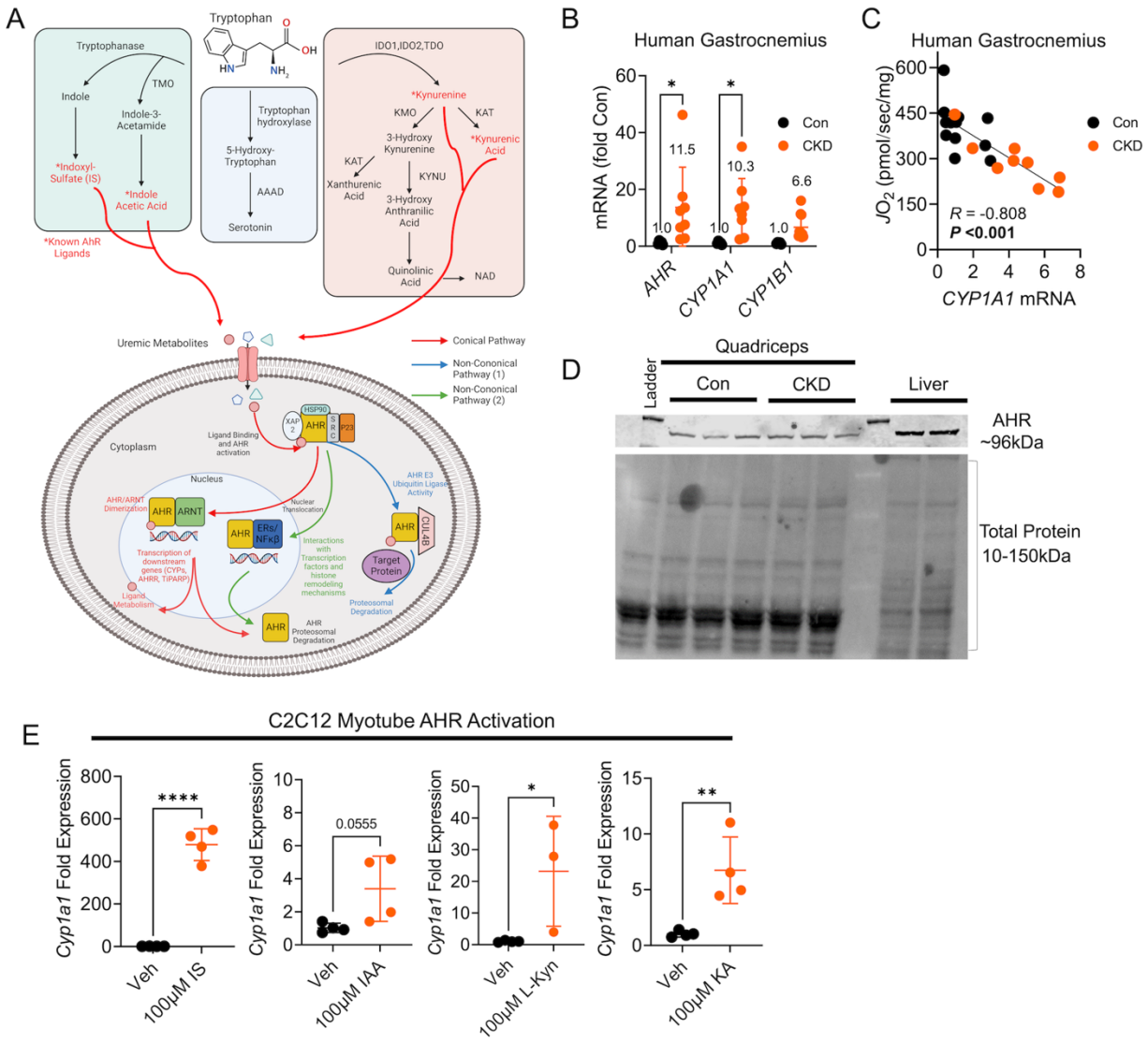


**Figure 1. AHR activation is present in CKD skeletal muscle and associates with mitochondrial respiratory function.** (A) Graphical depiction of tryptophan metabolism and the AHR signaling pathway. (B) qPCR quantification of *AHR*, *CYP1A1*, and *CYP1B1* mRNA signaling in gastrocnemius muscle biopsies from patients without (n=5) and with CKD (n=8-10). (C) Relationship between muscle mitochondrial oxygen consumption ($JO_2$) and *CYP1A1* patients with and without CKD. (D) Immunoblotting of the AHR protein in skeletal muscle of mice. (E) qPCR quantification of *Cyp1a1* mRNA levels in $C_2C_{12}$ myotubes treated with tryptophan-derived uremic metabolites indoxyl sulfate (IS), indole-3-acetic acid (IAA), L-kynurenine (L-Kyn), and kynurenic acid (KA), (n=3-4 biological replicates/group). Statistical analyses performed using two-tailed Student's *t*-test. Error bars represent the standard deviation. **P*<0.05, ***P*<0.01, *****P*<0.0001.

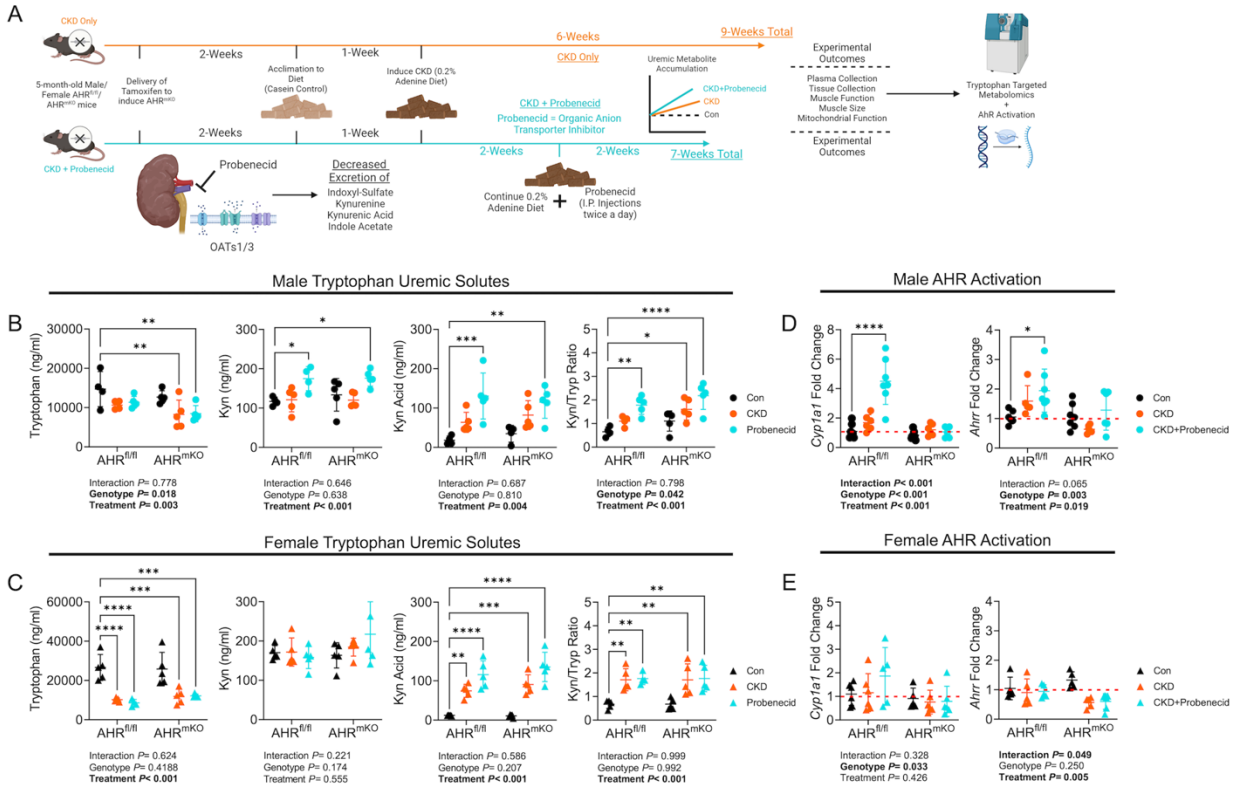


**Figure 2. Uremic metabolites accumulation drives AHR activation in CKD muscle which is abolished by muscle specific AHR deletion.** (A) Experimental treatment timeline. (B) Concentrations of tryptophan-derived uremic metabolites in plasma from male $AHR^{fl/fl}$ and $AHR^{mKO}$ mice without CKD, with CKD, and with CKD plus daily probenecid treatment (n=4-5/group/genotype). (C) Concentrations of tryptophan-derived uremic metabolites in plasma from female $AHR^{fl/fl}$ and $AHR^{mKO}$ mice without CKD, with CKD, and with CKD plus daily probenecid treatment (n=4-5/group/genotype). (D) qPCR quantification of *Cyp1a1* and *Ahrr* levels in skeletal muscle of male $AHR^{fl/fl}$ and $AHR^{mKO}$ mice without CKD, with CKD, and with CKD plus daily probenecid treatment (n=5-7/group/genotype). (E) qPCR quantification of *Cyp1a1* and *Ahrr* levels in skeletal muscle of female $AHR^{fl/fl}$ and $AHR^{mKO}$ mice without CKD, with CKD, and with CKD plus daily probenecid treatment (n=5-6/group/genotype). Statistical analyses performed using two-way ANOVA with Dunnett's post hoc testing for multiple comparisons. Error bars represent standard deviation. **P*<0.05, ***P*<0.01, ****P*<0.001, *****P*<0.0001.

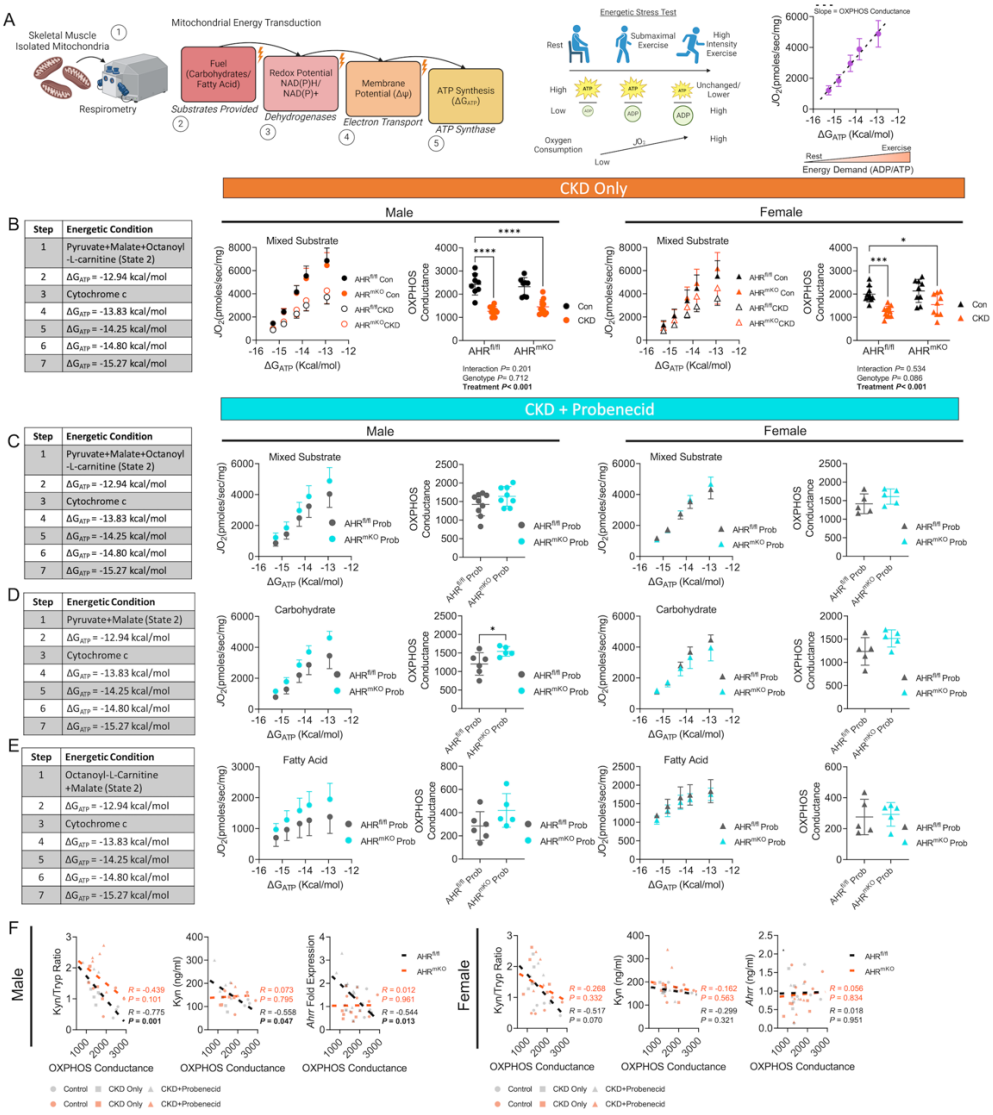


| Step | Energetic Condition |
|---|---|
| 1 | Pyruvate+Malate+Octanoyl -L-carnitine (State 2) |
| 2 | $\Delta G_{ATP}$ = -12.94 kcal/mol |
| 3 | Cytochrome c |
| 4 | $\Delta G_{ATP}$ = -13.83 kcal/mol |
| 5 | $\Delta G_{ATP}$ = -14.25 kcal/mol |
| 6 | $\Delta G_{ATP}$ = -14.80 kcal/mol |
| 7 | $\Delta G_{ATP}$ = -15.27 kcal/mol |

| Step | Energetic Condition |
|---|---|
| 1 | Pyruvate+Malate (State 2) |
| 2 | $\Delta G_{ATP}$ = -12.94 kcal/mol |
| 3 | Cytochrome c |
| 4 | $\Delta G_{ATP}$ = -13.83 kcal/mol |
| 5 | $\Delta G_{ATP}$ = -14.25 kcal/mol |
| 6 | $\Delta G_{ATP}$ = -14.80 kcal/mol |
| 7 | $\Delta G_{ATP}$ = -15.27 kcal/mol |

| Step | Energetic Condition |
|---|---|
| 1 | Octanoyl-L-Carnitine +Malate (State 2) |
| 2 | $\Delta G_{ATP}$ = -12.94 kcal/mol |
| 3 | Cytochrome c |
| 4 | $\Delta G_{ATP}$ = -13.83 kcal/mol |
| 5 | $\Delta G_{ATP}$ = -14.25 kcal/mol |
| 6 | $\Delta G_{ATP}$ = -14.80 kcal/mol |
| 7 | $\Delta G_{ATP}$ = -15.27 kcal/mol |

**Figure 3. Muscle specific AHR deletion improves mitochondrial OXPHOS with high tryptophan-derive uremic metabolite levels.** (A) Graphical depiction of mitochondrial OXPHOS system and the use of a creatine kinase clamp to measure oxygen consumption ($JO_2$) across physiologically relevant energetic demands ($\Delta G_{ATP}$). (B) Experimental conditions quantification $JO_2$ at each level of $\Delta G_{ATP}$, as well as the OXPHOS conductance in male and female $AHR^{fl/fl}$ and $AHR^{mKO}$ mice with or without CKD (n=8-12/group/genotype). Experimental conditions and quantification $JO_2$ at each level of $\Delta G_{ATP}$, as well as the OXPHOS conductance in male and female $AHR^{fl/fl}$ and $AHR^{mKO}$ mice with CKD plus daily probenecid treatment (n=5-9/group/genotype) for mixed substrates (C), pyruvate/malate (D), and octanoylcarnitine/malate (E). (F) Pearson correlational analyses of quantified OXPHOS conductance (mixed substrates) and kynurenine to tryptophan ratio, kynurenine concentrations, and *Ahrr* mRNA in male and female $AHR^{fl/fl}$ and $AHR^{mKO}$ mice across control, CKD, and CKD plus probenecid daily.

Data were analyzed by two-way ANOVA with Dunnett's post hoc testing for multiple comparisons in panel B. Two-tailed Student's *t*-test were performed in panels C-E. Error bars represent the standard deviation. *$P$<0.05, ***$P$<0.001, ****$P$<0.0001.

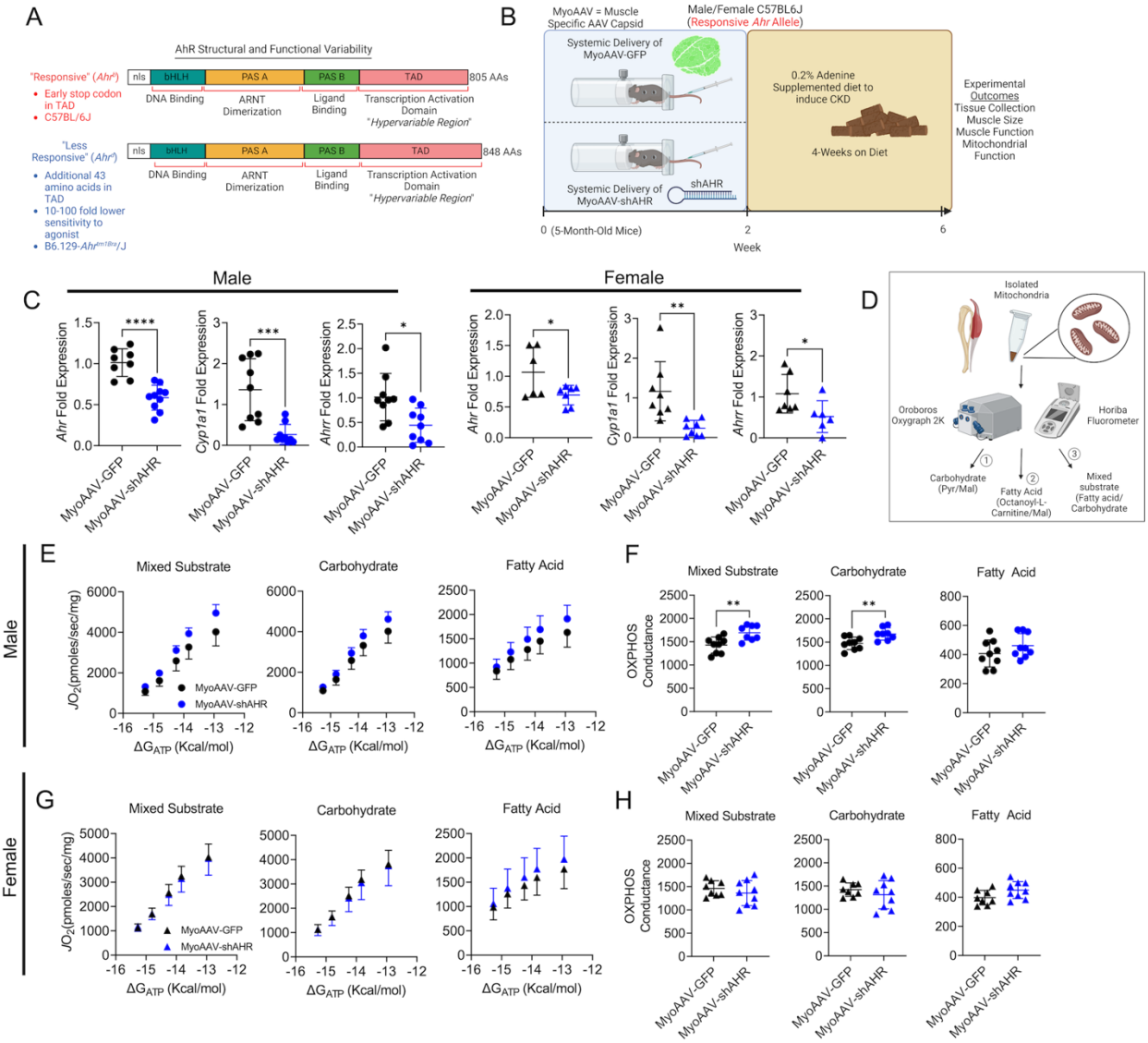


**Figure 4. Muscle-specific AHR knockdown improves mitochondrial OXPHOS in mice harboring the high-affinity AHR allele.** (A) Graphical depiction of polymorphisms in the AHR that confer differences in ligand affinity. (B) Experimental timeline of delivery of MyoAAV-GFP or MyoAAV-shAHR in high-affinity C57BL/6J mice with CKD. (C) qPCR validation of *Ahr* knockdown and subsequent reduction in *Cyp1a1* and *Ahrr* mRNA induction in MyoAAV-shAHR mice (n=6-10/group). (D) Graphical depiction of analytical approach for mitochondrial OXPHOS assessments. (E) Relationship between $JO_2$ and $\Delta G_{ATP}$ in isolated mitochondria from the gastrocnemius muscle in different substrate conditions in male mice with CKD (n=8-9/group). (F) Quantification of OXPHOS conductance in male mice (n=8-9/group). (G) Relationship between $JO_2$ and $\Delta G_{ATP}$ in isolated mitochondria from the gastrocnemius muscle in different substrate conditions in female mice with CKD (n=8-9/group). (H) Quantification of OXPHOS conductance in

female mice (n=8-9/group). Statistical analyses were performed using two-tailed Student's *t*-test. Error bars represent standard deviation. *$P$<0.05, **$P$<0.01, ***$P$<0.001, ****$P$<0.0001.

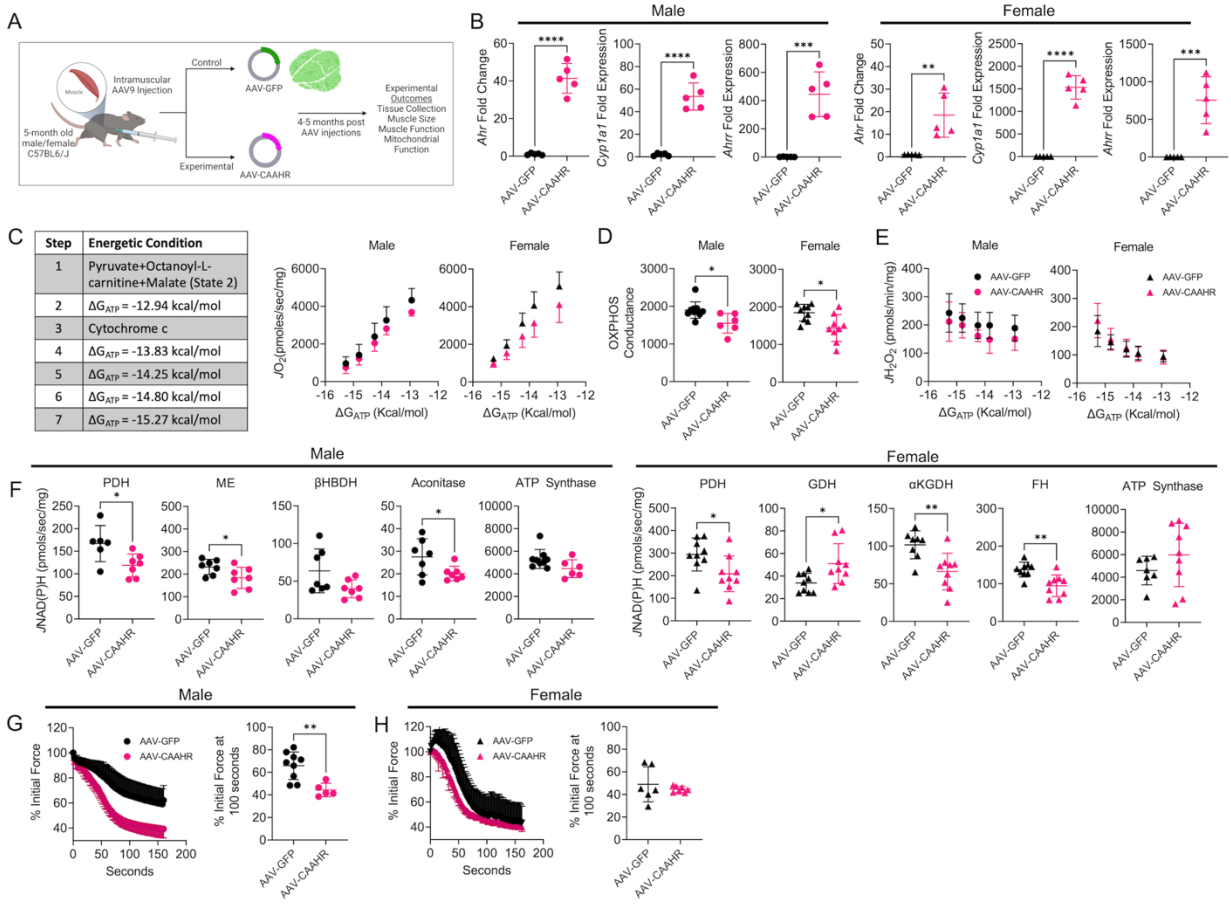


**Figure 5. Ectopic expression of a constitutively active AHR impairs muscle mitochondrial OXPHOS in mice with normal kidney function.** (A) Experimental design for muscle-specific delivery of mutant constitutively active AHR (CAAHR). (B) qPCR of *Ahr*, *Cyp1a1*, and *Ahrr* in male and female mice treated with AAV-GFP and AAV-CAAHR (n=5/group). (C) Substrate conditions and quantification of the relationship between $JO_2$ and $\Delta G_{ATP}$ in male and female mice treated with AAV-GFP or AAV-CAAHR (n=6-10/group). (D) OXPHOS conductance in male and female mice (n=6-10/group). (E) Mitochondrial $JH_2O_2$ and $\Delta G_{ATP}$ in male and female mice (n=6-10/group). (F) Quantification of mitochondrial matrix dehydrogenase enzyme activity in male and female mice (n=6-9/group). (G) Analysis of extensor digitorum longus muscle fatigue in male and female mice (n=5-9/group). Data analyzed using two-tailed Student's *t*-test. Error bars represent standard deviation. *$P$<0.05, **$P$<0.01, ***$P$<0.001, ****$P$<0.0001.

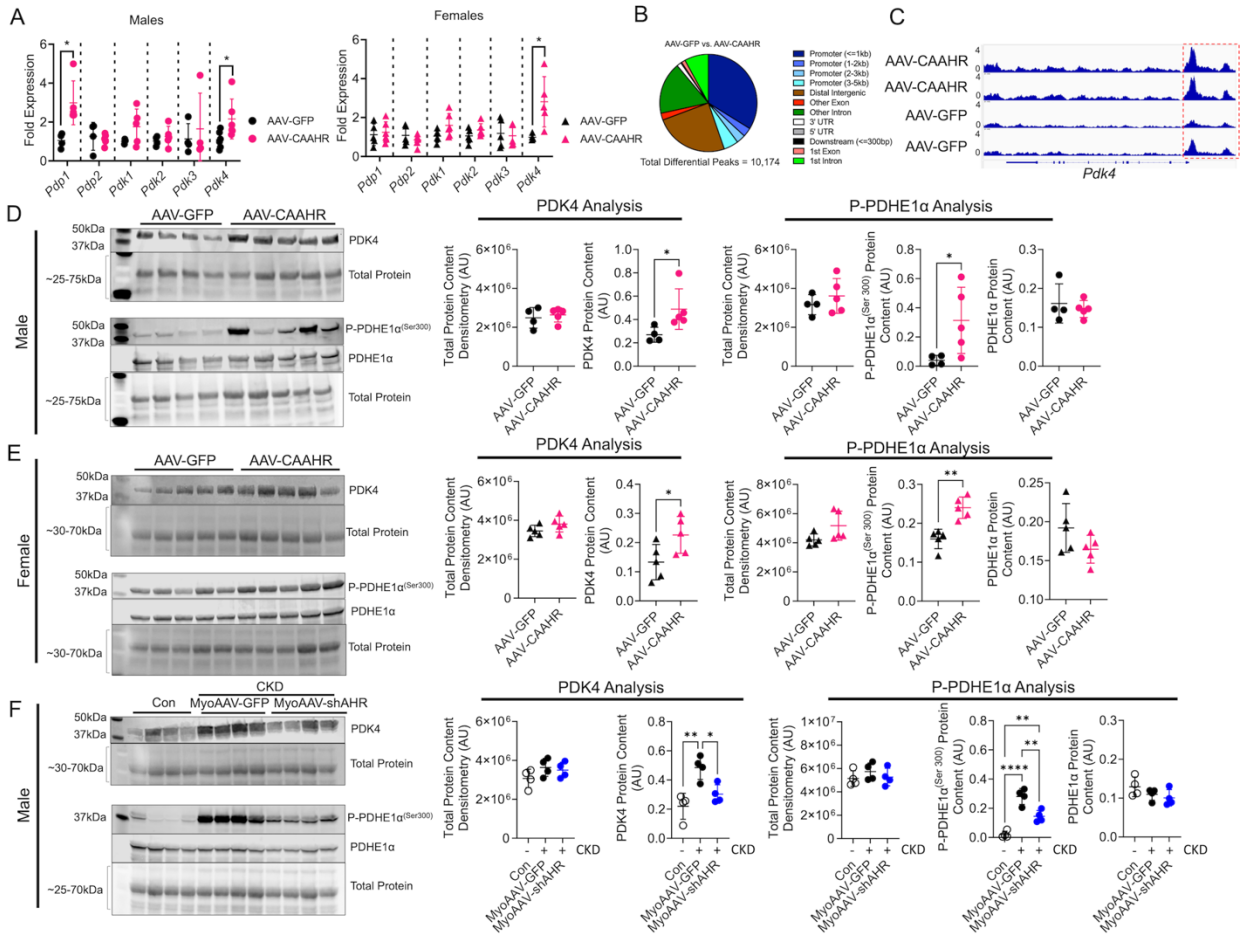

**Figure 6. AHR activation increased PDK4 expression and PDH phosphorylation.** (A) qPCR of *Pdp1*, *Pdp2*, *Pdk1*, *Pdk2*, *Pdk3*, and *Pdk4* in male and female mice treated with AAV-GFP and AAV-CAAHR (n=5-6/group). (B) Peak annotation pie charts for ATAC-Seq peaks in AAV-GFP vs. AAV-CAAHR muscles (n=3/group). (C) IGV snapshots of the *Pdk4* gene showing chromatin accessibility with the red-dashed box highlighting the promoter region. (D) Western blotting of PDK4, phosphorylated PDHE1α$^{Ser300}$, and total PDHE1α protein expression in male AAV-GFP or AAV-CAAHR gastrocnemius muscle (n=4-5/group). (E) Western blotting of PDK4, phosphorylated PDHE1α$^{Ser300}$, and total PDHE1α protein expression in female AAV-GFP or AAV-CAAHR gastrocnemius muscle (n=5/group). (F) Western blotting of PDK4, phosphorylated PDHE1α$^{Ser300}$, and total PDHE1α protein expression in male control, CKD MyoAAV-GFP, and CKD MyoAAV-shAHR gastrocnemius muscle (n=4/group). Data in panels A, D, and E were analyzed using two-tailed Student's *t*-test. Data in Panel F were analyzed using one-way ANOVA with Tukey's post-hoc. **P*<0.05, ***P*<0.01, *****P*<0.0001.

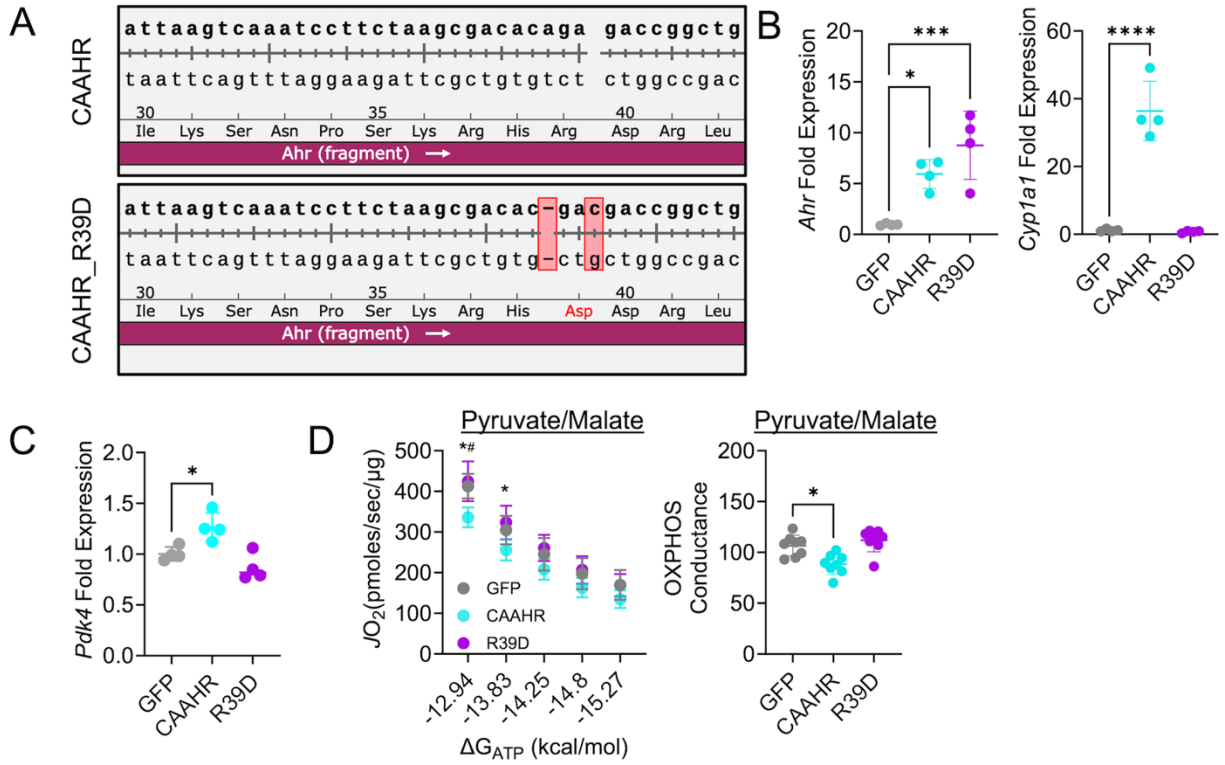


**Figure 7. Expression of a transcriptionally inept CAAHR abolishes Pdk4 expression and pyruvate supported OXPHOS impairment in $C_2C_{12}$ muscle cells.** (A) Sequencing results demonstrating the introduction of point mutation that converted arginine-39 to aspartate (R39D). (B) qPCR validation of the overexpression of *Ahr* and lack of transcriptional activity (*Cyp1a1*) in the R39D mutant. A GFP control plasmid was also tested. (n=4/group) (C) *Pdk4* mRNA expression (fold GFP). (n=4/group) (D) Pyruvate supported respiration in muscle cells and quantified OXPHOS conductance. (n=8/group). Error bars represent standard deviation. Data were analyzed using one-way ANOVA with Tukey's post-hoc. **P*<0.05, ***P*<0.01, ****P*<0.001, *****P*<0.0001. #*P*<0.05 for CAAHR vs. R39D.